



Molecular Orientation and Nanoscale Morphology- Property Relations in Organic Semiconductors for Photovoltaics

Insights from NEXAFS Spectroscopy and Scanning
Probe Microscopy

Leticia Christopholi

Faculty of Health, Science and Technology

Physics

DOCTORAL THESIS | Karlstad University Studies | 2026:23

Molecular Orientation and Nanoscale Morphology- Property Relations in Organic Semiconductors for Photovoltaics

Insights from NEXAFS Spectroscopy and Scanning
Probe Microscopy

Leticia Christopholi

Molecular Orientation and Nanoscale Morphology-Property Relations in Organic Semiconductors for Photovoltaics
- Insights from NEXAFS Spectroscopy and Scanning Probe Microscopy

Leticia Christopholi

DOCTORAL THESIS

Karlstad University Studies | 2026:23

urn:nbn:se:kau:diva-109204

ISSN 1403-8099

ISBN 978-91-7867-694-1 (print)

ISBN 978-91-7867-695-8 (pdf)

<https://doi.org/10.59217/ybig4492>

© The author

Distribution:
Karlstad University
Faculty of Health, Science and Technology
Department of Engineering and Physics
SE-651 88 Karlstad, Sweden
+46 54 700 10 00

Print: Universitetstryckeriet, Karlstad 2026

*"O correr da vida embrulha tudo. A vida é assim: esquenta, esfria,
aperta e daí afrouxa, sossega e depois desinquieta. O que ela quer da
gente é coragem."*

— João Guimarães Rosa, Grande Sertão: Veredas (1956)

Abstract

Organic solar cells (OSCs) are part of an emerging renewable energy technology that offers a low-cost, flexible, and lightweight alternative to conventional photovoltaics. Record power conversion efficiencies of OSCs have exceeded 20% to date. With the continuous development of new electron donor and acceptor materials through molecular design, new challenges arise in controlling and characterizing the active layer morphology.

This thesis addresses these challenges by investigating the factors that govern the molecular orientation and nanostructure in donor-acceptor systems, while critically evaluating the strengths and limitations of the applied characterization techniques. Angular dependent Near-Edge X-ray Absorption Fine Structure (NEXAFS) spectroscopy of spin-coated films of Y-type small molecule acceptors revealed that solvent-solute interactions strongly influence molecular orientation during film formation, with chloroform promoting preferential face-on orientation of the Y-type acceptor, while less suitable solvents led to pre-aggregation and non-oriented films.

This study was extended to polymer acceptors and donor-acceptor blends. Nitrogen K-edge NEXAFS spectroscopy was introduced as an element-selective probe that enables component-specific determination of molecular orientation of the acceptor polymer in multicomponent systems, as well as depth-dependent analysis through complementary detection modes. Moreover, the sulfur L₁-edge was evaluated as a sulfur-selective probe for thiophene-based semiconductors, not only for molecular orientation analysis but also for unveiling aspects of the underlying electronic structure, thereby providing a basis for future studies of charge dynamics.

Sequential deposition was explored as a strategy to control vertical phase separation, enabling inversion of donor-acceptor stratification while preserving molecular orientation.

Finally, complementary AFM-based techniques were applied to correlate nanoscale morphology in donor-acceptor blend films with local mechanical and electrical properties, highlighting both the capabilities and challenges in the interpretation of such results for finally mixed non-fullerene-based blends.

Overall, this work emphasizes that understanding morphology in organic solar cells requires combining element-selective spectroscopy with nanoscale characterization methods. These results advance the understanding of how processing conditions govern molecular orientation and nanoscale structure, while establishing a more robust framework for probing these properties in complex organic photovoltaic systems.

Sammanfattning

Organiska solceller (OSC:er) utgör en del av en framväxande förnybar energiteknik som erbjuder ett alternativ till konventionell fotovoltaik med låg kostnad, samtidigt som dessa solceller är flexibla och har låg vikt. Rekordhöga verkningsgrader rörande effekten för OSC:er överstiger idag 20 %. Med den kontinuerliga utvecklingen av nya elektrondonator- och acceptormaterial genom molekylär design uppstår nya utmaningar när det gäller att kontrollera och karakterisera morfologin i det aktiva lagret.

Denna avhandling behandlar dessa utmaningar genom att undersöka de faktorer som styr den molekylära orienteringen och nanostrukturen i donator–acceptorsystem, samtidigt som styrkorna och begränsningarna hos de använda karakteriseringsteknikerna kritiskt utvärderas. Vinkelberoende Near-Edge X-ray Absorption Fine Structure (NEXAFS)-spektroskopi på spincoatade filmer av småmolekylära acceptorer av Y-typ visade att interaktioner mellan det lösta ämnet och lösningsmedlet starkt påverkar den molekylära orienteringen under filmbildningen, där kloroform främjade en preferentiell face-on-orientering hos acceptorn av Y-typ, medan andra lösningsmedel ledde till en mindre lämplig preaggregering och icke-orienterade filmer.

Studien utvidgades till polymeracceptorer och donator–acceptorblandningar. NEXAFS-spektroskopi vid kvävet K-kant introducerades som en elementsektiv prob som möjliggör komponentspecifik bestämning av den molekylära orienteringen hos acceptorpolymeren i multikomponentsystem, samt djupberoende analys genom komplementära detektionsmoder. Vidare utvärderades svavlets L1-kant som en svavelsektiv prob för tiofenbaserade halvledare, inte bara för

analys av molekylär orientering utan också för att belysa aspekter av den underliggande elektroniska strukturen, och därmed skapa en grund för framtida studier av laddningsdynamik.

Sekventiell deposition undersöktes som en strategi för att kontrollera vertikal fassetparation, vilket möjliggjorde en inversion av donator–acceptor-stratifieringen samtidigt som den molekylära orienteringen bevarades.

Slutligen tillämpades komplementära AFM-baserade tekniker för att korrelera morfologin på nanoskala i filmer av donator–acceptorblandningar med lokala mekaniska och elektriska egenskaper, vilket belyser både möjligheterna och utmaningarna i tolkningen av sådana resultat för fint blandade icke-fullerenbaserade filmer.

Sammantaget betonar detta arbete att förståelsen av morfologi i organiska solceller kräver en kombination av elements selektiv spektroskopi och karakteriseringsmetoder på nanoskala. Dessa resultat ger möjlighet till ökad förståelse för hur processbetingelser styr molekylär orientering och struktur på nanoskala, samtidigt som de etablerar ett mer robust ramverk för att undersöka dessa egenskaper i komplexa organiska fotovoltaiska system.

List of Publications

The following publications are included in this thesis:

Paper 1

Role of the solvent on the orientation of Y-Type Acceptor Molecules in Spin-Coated Films.

Leticia P. Christopholi, Cleber F. N. Marchiori, Ishita Jalan, Andreas Opitz, Stela Andrea Muntean, Ellen Moons.

The Journal of Physical Chemistry C 128.42 (2024): 17825-17835.

Paper 2

Probing molecular orientation of donors and acceptors in all polymer blends by Near-Edge X-Ray Absorption Fine Structure Spectroscopy

Leticia P. Christopholi, Zewdneh Genene, Cleber F. N. Marchiori, Stela Andrea Muntean, Ergang Wang, Ellen Moons

Journal of Physics: Materials. 9 (2026) 025001

Paper 3

Sequential Deposition Enables Suppression of Spontaneous Donor Enrichment of the Surface in Spin-coated Films

Leticia P. Christopholi, Paweł Dąbczyński, Saurabh Pareek, Ewa Partyka – Jankowska, Marcin Zając, Stela Andrea Muntean, Ellen Moons

Journal of Physics: Materials. 9 (2026) 015018

Paper 4

Unravelling Sulphur L₁-Edge NEXAFS Spectra of Thiophene-based Organic Semiconductors

Leticia P. Christopholi, Robert Temperton, Alexei Preobrajenski, Stela Andrea Muntean, Ellen Moons, Cleber F. N. Marchiori

Manuscript

Paper 5

Challenges and Opportunities of Probing Surface Photovoltage, Photocurrent, and Mechanical Properties at the Nanoscale in PBDB-T:Y6 Films for Organic Photovoltaics

Leticia P. Christopholi, Ismail Benamar, Stela Andrea Muntean, Philippe Leclere and Ellen Moons

Manuscript

Papers not included in this thesis:

Paper 6

From blend to bilayer: solvent-controlled vertical stratification and orientation in PM6/PYIT films.

Saurabh Pareek, Paweł Dąbczynski, Leticia P. Christopholi, Ewa Partyka Jankowska, Marcin Zajac, Cleber F. N. Marchiori, Leif Ericsson, and Ellen Moons

Manuscript

The author's contribution to the publications

Paper 1: I was responsible for sample preparation and contributed to the sample characterization. This included performing atomic force microscopy (AFM), UV-vis spectroscopy, and near-edge X-ray absorption fine structure (NEXAFS) spectroscopy measurements as part of the team. I analyzed the data and contributed to the scientific discussions. I wrote the first manuscript draft, implemented revisions based on the feedback from co-authors, and finalized the manuscript.

Paper 2: I was responsible for sample preparation, and I was part of the team for the sample characterization by NEXAFS spectroscopy measurements and data analysis. I wrote the first manuscript draft, implemented revisions based on the feedback from co-authors, and finalized the manuscript.

Paper 3: I was responsible for sample preparation and contributed to sample characterization. This included performing AFM and NEXAFS spectroscopy measurements as part of the team. I was responsible for the data analysis of AFM and NEXAFS and contributed to the analysis

of Time-of-Flight Secondary Ion Mass spectrometry (ToF-SIMS) data. I wrote the first manuscript draft, implemented revisions based on the feedback from co-authors, and finalized the manuscript.

Paper 4: I was responsible for sample preparation, and I was part of the team for the sample characterization by NEXAFS spectroscopy measurements. I wrote the first manuscript draft, implemented revisions based on the feedback from co-authors, and finalized the manuscript

Paper 5: Prepared all the samples and performed a part of the characterization by AFM and other SPM techniques, part of which was done in the group of Prof. Philippe Leclere at LPNE at UMons. I wrote the first manuscript draft, implemented revisions based on the feedback from co-authors, and finalized the manuscript.

Acknowledgments

I would like to express my deepest gratitude to my supervisor, Ellen Moons, and co-supervisor, Stela Andrea Muntean, for their invaluable guidance, support, encouragement, and patience throughout this journey. I feel incredibly fortunate to have had the mentorship of two brilliant women who have inspired and motivated me through the challenges of this exciting but demanding path. Their support went far beyond academic supervision, and in the toughest moments of this journey, they were always there with caring words and a shoulder to cry on.

I extend my sincere thanks to Cleber Marchiori, Paulo Marchezi, and Leif Ericsson, for their unwavering scientific support and collaboration, which have been integral to the progress of my work.

I am also grateful to my colleagues at the Department of Engineering and Physics for making my time here pleasant.

I would like to thank our dear chemists, Ishita Jalan and Jan van Stam, whose collaboration and contributions made this work what it is.

I would like to thank my collaborators, Phillippe Leclere and Ismail Benamar, at the University of Mons (UMons) for hosting me during the research visits and introducing me to advanced scanning probe microscopy techniques. Without this collaboration, an important part of this thesis would not have been possible. In addition, I would like to thank the travel grant from The Royal Swedish Academy of Sciences for the work carried out at UMons.

I am grateful to the Swedish Research Council for the project funding (grant nr.2021-04798).

To my family, thank you for always supporting my dreams and standing by my side through the highs and lows. Your love and belief in me have been my anchor.

I wish to thank my friends outside the university for their companionship and love, which have made this time away from my home and loved ones in Brazil less lonely and so much brighter. More than friends, I found more than one family here. At the end of this journey, and while facing unexpected disappointments in life, I came to realize how deep the connections I built truly are. They were there for me in both good times and bad, and when I needed support the most, they carried me through and took care of me. And I know these are friendships that will last for a lifetime.

Finally, I am also grateful for the resilience I found in myself throughout this process. Looking back, this work reflects not only scientific development but also personal growth, resilience, and perseverance. Years ago, the younger Leticia could not have imagined all that she would achieve, the places she would see, or that one day she would be fluent in English. To that younger version of myself, I would simply say: I am proud of how far we have come.

Contents

ABSTRACT	II
SAMMANFATTNING	IV
LIST OF PUBLICATIONS	VI
THE AUTHOR'S CONTRIBUTION TO THE PUBLICATIONS	VII
ACKNOWLEDGMENTS	IX
1 INTRODUCTION	1
2 ORGANIC PHOTOVOLTAICS	6
2.1 Organic semiconductors	6
2.2 Physics of Organic Solar Cells	8
2.3 Morphology of the photoactive layer	13
2.3.1 Sequential deposition.....	15
2.3.2 Thermodynamic aspects of phase separation in polymer blends.....	17
2.3.3 Molecular Orientation in Conjugated Organic Semiconductor Films.....	21
3 MATERIALS AND SAMPLE PREPARATION	24
3.1 Polymer donor PBDB-T and PM6	25
3.2 Small molecules Y5 and Y6	27
3.3 Polymer acceptors PF5-Y5 and PYT.....	28
3.4 Sample preparation	29
3.4.1 Spin-coating for film deposition.....	29
4 CHARACTERIZATION TECHNIQUES	32
4.1 Atomic force microscopy	32
4.1.1 PeakForce quantitative nanomechanical mapping.....	34
4.1.2 Kelvin Probe Force Microscopy	37
4.1.3 Photoconductive Atomic Force Microscopy	40
4.1.4 Atomic force microscopy – infrared spectroscopy	42
4.2 Near-edge X-ray absorption fine structure spectroscopy.....	44
4.3 Time-of-flight secondary ion mass spectrometry (ToF-SIMS)	50
5 SUMMARY OF THE PUBLICATIONS	52
5.1 Paper 1	52
5.2 Paper 2	53
5.3 Paper 3	54
5.4 Paper 4	55
5.5 Paper 5	56
6 CONCLUSION AND OUTLOOK	57

7 REFERENCES	60
LIST OF ABBREVIATIONS AND ACRONYMS	67

1 Introduction

In the face of growing global energy demands and the pressing need to mitigate the most detrimental scenarios of climate change, the need for utilizing sustainable and renewable energy sources has never been more critical. According to the “World Energy Outlook 2025” report by the International Energy Agency (IEA), 79% of the world’s primary energy supply is still derived from fossil fuels [1]. Additionally, the strong rebound in economic activity and CO₂ emissions following the COVID-19 pandemic, followed by the energy crisis triggered by the Russian invasion of Ukraine, has aggravated climate change by accelerating CO₂ emissions and temperature rise [2]. Within this context, limiting global warming to 1.5 °C above the pre-industrial levels has become urgent. Even in the IEA’s Net Zero Roadmap¹ scenario, global temperatures are projected to temporarily rise to approximately 1.65 °C before declining to 1.5 °C by 2100. However, returning warming to 1.5 °C will only be possible through immediate reduction in greenhouse gas² emissions. These projections highlight the urgent necessity of accelerating the transition from fossil fuels to renewable energy systems.

On the other hand, in Europe, the urgent need to reduce dependence on Russian gas has boosted the green transition. Solar energy has great potential to be one of the main players in the electrification of society. The Sun is the most abundant energy resource on Earth – 173000 terawatts of energy strikes the Earth continuously. That’s more than 10000 times the world’s total energy needs. In contrast, for example, wind as a resource has a potential of 4000 GW [3]. In addition to its vast theoretical potential, solar photovoltaics (PV) have recently become the leading renewable energy source in terms of installed capacity [4]. However, the rapid expansion of manufacturing has led to significant overcapacity, resulting in sustained price reductions and increased pressure across the photovoltaic industry [5].

¹ The Net Zero road map is a strategic plan aimed at reducing greenhouse gas emissions to net zero by a specific target year, nowadays 2050.

² Greenhouse gases are gases that trap heat in the atmosphere including carbon dioxide, methane, nitrous oxide and fluorinated gases.

Specifically, in terms of electricity production, solar energy can be converted directly into electricity by the photovoltaic effect³. The first photovoltaic device was a silicon solar cell invented by researchers at Bells laboratories in 1954, with 4,5% efficiency [6]. Since then, photovoltaic devices have evolved, and different types of technologies have been developed. Currently, wafer-based crystalline silicon (c-Si) technologies account for more than 98% of the overall cell production; the single crystalline cells, feature commercial efficiencies between 20% and 25% [7]. A major development in photovoltaic research is the integration of perovskite absorber with c-Si in tandem devices. Perovskite/silicon tandem solar cells have achieved record efficiencies exceeding 33%, demonstrating significant potential to surpass the theoretical limits of single-junction silicon cells [8].

Organic solar cells (OSCs), classified among the third generation, have attracted considerable attention as lightweight, mechanically flexible, and potentially low-cost photovoltaic devices [9]. Typically, an OSC consists of a photon absorber layer (active layer), sandwiched between two electrodes. The active layer is composed of polymers and/or small molecules that act as electron donors and acceptors. The concept of OSCs was first introduced in 1959 by Kallmann and Pope with a single-layer device [10]. They used an anthracene single crystal as the active layer placed between two metal electrodes with different work functions. However, at the time, single-layer devices had very low efficiencies (<1%), due to not only the low dielectric constant of the organic semiconductors, which limited exciton dissociation, but also to the narrow absorption range of anthracene in the visible spectrum. Excitons, which are electron-hole pairs created when light is absorbed, need to be efficiently dissociated into charge carriers to generate electrical current.

Then, in 1986, Tang introduced the organic bilayer or planar heterojunction (PHJ), where the active layer was composed of two different

³ The photovoltaic effect consists in the process by which light is converted into electricity. This phenomenon was discovered in 1839 by the French physicist, Alexandre Emond Becquerel.

materials, i.e. electron donor and electron acceptor materials [11]. The built-in electric field, resulting from the energy level offset between donor and acceptor materials, promoted a more efficient exciton dissociation. However, there was still another issue to face: the exciton diffusion length. The exciton had to travel distances exceeding their diffusion length to reach the donor/acceptor interface, leading to significant charge recombination and resulting in low conversion efficiencies. A major breakthrough came with the discovery of ultrafast photoinduced charge transfer between conjugated polymers and fullerene derivatives by Sariciftci and co-workers [12], demonstrating that efficient charge separation could occur at donor-acceptor interfaces on ultrafast time-scales. This finding highlighted the importance of maximizing interfacial area within the active layer. After that, another breakthrough was the introduction of the bulk heterojunction (BHJ) by Heeger's group and Friend's group [13, 14]. The bulk heterojunction consists of a donor-acceptor blend with a phase-separated nanostructure that provides a high interfacial area for charge separation. The bulk heterojunction is now known as the conventional OSC device.

Recently, looking for further morphology optimization of the active layer to achieve the ideal bulk heterojunction, researchers started to explore the sequential deposition method [15]. Unlike bulk heterojunction, which exhibits disordered morphology, the goal here is to create an intermixed donor-acceptor region sandwiched between donor-rich and acceptor-rich phases. Additionally, researchers have been working on synthesizing organic semiconductors with a higher dielectric constant, which reduces the exciton binding energy. However, the higher dielectric constant can lead to compatibility issues during the solution processing due to the increased polarity of the materials. Nevertheless, it is expected that shortly, with the development of materials with very high dielectric constant, efficient single-layer organic devices will be a possibility. The historical evolution of the OSC structure and current prospects reveal a tendency to revisit the early structures but with advanced materials based on what has been learned so far (Figure 1).

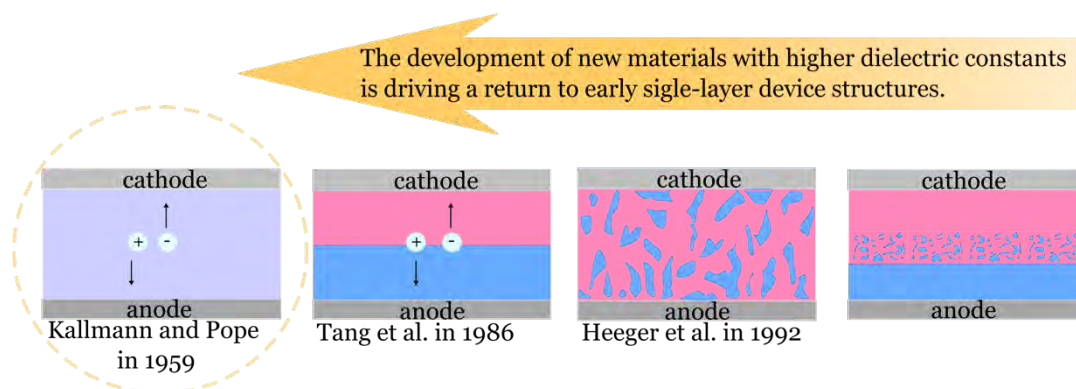


Figure 1. Overview of OSCs structure evolution and prospects.

In recent years, power conversion efficiencies exceeding 20% have been achieved through advances in non-fullerene acceptor-based systems, together with continued optimization of device architecture, processing conditions, and interlayers, in particular the hole-transport layer [16-21]. While this marks significant progress compared to earlier OSCs, these efficiencies remain lower than those of commercialized silicon solar cells, which can exceed 26%. Rather than replacing silicon technology, OSCs have the potential to complement it by offering advantages such as flexibility, lightweight designs, solution processability, and compatibility with a wide range of applications, and by being integrated with silicon in tandem solar cells. Progress in the field of OSCs depends on various key factors, some of which are: i) the design and synthesis of new organic semiconductors, ii) transition to more environmentally friendly solvent iii) the optimization of the device structure, iv) the deep understanding of device physics, v) operational stability, vi) upscaling and vii) fabrication costs [22, 23]. Specifically, regarding aspect iii), morphology plays an important role in determining the efficiency of the device. For example, in the case of the conventional BHJ, the arrangement and distribution of donor and acceptor materials within the active layer influence the pathways for charge transport and the efficiency of the exciton dissociation.

For solution-processed OSCs, controlling morphology involves considering the intrinsic properties of donor and acceptor materials as well as parameters used for film processing. Researchers have employed strategies such as solvent choice, solvent additives, annealing conditions

(thermal and solvent vapor), spin-coating speed, and concentration of the active layer solution to fine-tune the nanoscale arrangement and phase-separation of materials. Optimizing the morphology relies on the ability to resolve the structural and compositional properties on the nanoscale, which requires advanced characterization techniques, such as Atomic Force Microscopy (AFM), Transmission Electron Microscopy (TEM), Scanning Electron Microscopy (SEM), Time-of-Flight Ion mass spectrometry (ToF-SIMS), Grazing Incidence Wide Angle X-ray scattering (GIWAXS), and Near Edge X-ray Spectroscopy (NEXAFS). When combined, these techniques can provide detailed insights into nanoscale morphology, material distribution, and molecular orientation.

With the available characterization techniques, resolving nanoscale morphology and its relation to nanoscale electronic properties remains challenging in multicomponent donor-acceptor blends, in the context of the rapid advances in materials design. While several methods provide structural or compositional information, a critical understanding of the strengths and limitations of each technique is required to extract meaningful structure-property relationships.

The overall goal of this thesis is to advance the understanding of how processing parameters influence the final morphology of the active layer in organic solar cells, with particular emphasis on molecular orientation. A central objective is to investigate how the choice of solvent, deposition method, and post-treatments affects the final molecular orientation of individual materials in multicomponent donor-acceptor systems. It also aims to investigate how nanoscale morphology and local photovoltaic response vary across the active layer, allowing the identification of inhomogeneities in photocurrent generation that are not accessible from macroscopic device measurements. Finally, the thesis aims to establish a more robust framework for probing these properties in modern organic photovoltaic systems by evaluating the strengths, limitations, and opportunities of advanced characterization techniques.

2 Organic Photovoltaics

2.1 Organic semiconductors

Organic semiconductors are carbon-based materials that rely on conjugated π electron systems for electronic conduction. π -electron systems arise from the overlap of p orbitals and may be localized or delocalized between adjacent atoms. Delocalization is commonly observed in conjugated molecules with alternating single and double bonds. To understand the distinct electrical properties of organic semiconductors, one can start by examining the electronic structure of carbon. Carbon in its elementary form has 6 electrons, which are distributed in the electronic structure as $1s^2$, $2s^2$, $2p^2$. However, when bonding to other atoms, a lower energy state is achieved by the hybridization between $2s$ and $2p$ atomic orbitals. Hybridization involves the combination of one s orbital and one, two, or three p orbitals to form new hybrid orbitals sp^1 , sp^2 , and sp^3 , respectively [24]. These different hybridizations lead to the formation of different types and numbers of bonds, specifically π and σ . The molecular orbitals (MOs) associated with π and σ bonds are formed through the linear combination of atomic orbitals. These orbitals arise from constructive or destructive overlap of atomic orbitals, resulting in bonding (lower energy) or antibonding (higher energy) character [24].

Let's consider the examples of ethane (C_2H_6), ethene (C_2H_4), and ethyne (C_2H_2) to illustrate this (Figure 2). In the case of ethane (Figure 2.a), each carbon atom undergoes sp^3 hybridization, forming four σ bonds; three of them with hydrogen atoms and one with the other carbon atom. On the other hand, ethene (Figure 2.b) is formed through the sp^2 hybridization of each carbon atom, which results in three σ bonds and one π bond; two of those σ bonds with hydrogen and one σ and one π bond between the carbon atoms. In the case of ethyne (Figure 2.c), each carbon undergoes sp^1 hybridization, resulting in two π bonds between carbon atoms: one σ bond with the other carbon and one σ bond with hydrogen. Additionally, Figure 2.d shows the MOs energy diagram for the ethene molecule; the overlapping of two unhybridized $2p_z$ atomic orbitals results in a bonding π molecular orbital (π MO) and one antibonding π^* MO. In the case of this molecule, the highest

occupied molecular orbital (HOMO) is the π MO, and the lowest unoccupied molecular orbital (LUMO) π^* MO. The electronic structure of Ethene will be revisited in section 4.2, as an example to discuss a characterization technique that provides information about electronic structure and molecular orientation. Ethene is also a fundamental building block in conjugated systems, such as the benzene ring, which forms the basis of many aromatic molecules and conjugated polymers

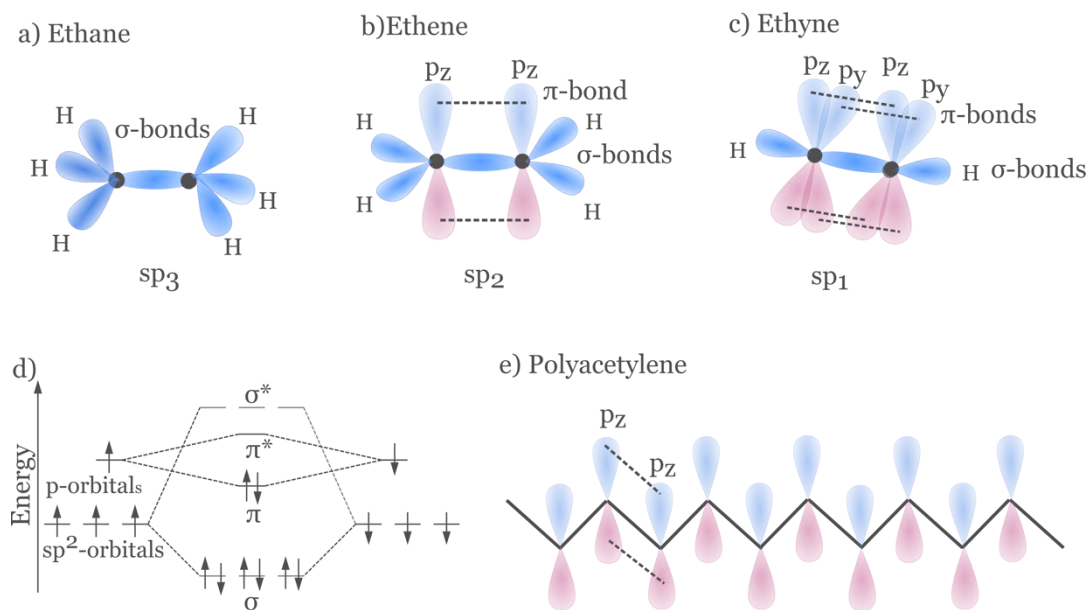


Figure 2. Molecules formed by the combination of two carbons and different numbers of hydrogen atoms, depending on the degree of hybridization a) ethane, when the two carbon atoms undergo sp^3 hybridization, b) ethene, in the case of sp^2 hybridization, and c) ethyne in the case of sp^1 hybridization d) shows the energy MOs diagram of ethene, for exemplification. In e) a simplified polyacetylene structure (double bonds and hydrogen atoms are not shown) shows the p_z orbitals located perpendicular to the trigonal plane, which overlap forming the π -system; in this configuration, the electrons are delocalized and loosely bound.

Ethene, also known as ethylene, is the building block for polyacetylene, one of the first and simplest conjugated polymers [25]. The conjugated carbon chain, characterized by the alternating single and double-bond structure, is the distinguishing feature of all conductive polymers and molecules [26]. To promote the formation of the polyacetylene, each carbon atom undergoes sp^2 hybridization. Three of the four valence electrons form σ bonds: two between carbon atoms and one with a hydrogen atom. The fourth electron is located in the p_z orbital of each

carbon atom. The overlapping of the p_z orbitals from each carbon atom forms the π -system, which extends above and below the sp^2 . In this configuration, the π system is half-filled (one electron per carbon atom), leading to the expectation that polyacetylene would behave as a metal. However, as predicted by Peierls, such a one-dimensional half-filled system is unstable due to the interaction between electrons and phonons within the polymer [26].

To achieve a more stable configuration, the polymer adopts a structure with alternating longer single and shorter double bonds along the chain. This results in the formation of bonding (π) and antibonding (π^*) that are separated by an energy gap (around 1.5 eV for *trans*-polyacetylene [27]), which gives rise to its semiconducting behavior. This energy gap, corresponding to the difference between the highest occupied and lowest unoccupied molecular orbitals, is typically in the range of 1-3 eV for organic semiconductors [28].

The electronic structure and, consequently, resulting properties of organic semiconductors are rather complex. The role of conjugation in one-dimensional polymers, such as polyacetylene, has been extensively studied, as the delocalization of π -electrons along the polymer backbone is crucial for enabling efficient charge transport and electronic conductivity. However, predicting the final electronic structure of more complex structures that would include other atoms such as oxygen, nitrogen, and sulfur is not as straightforward.

2.2 Physics of Organic Solar Cells

In the previous section, the electronic structure of organic semiconductors was described as a carbon-based π -conjugated system, characterized by an energy gap between the HOMO and LUMO of the material. Despite the semiconducting properties, organic semiconductors differ significantly from inorganic semiconductors. In particular, light absorption in organic semiconductors typically leads to the formation of strongly bound electron-hole pairs, known as excitons, rather than free charge carriers. In inorganic semiconductors, exciton binding energies are low, and thermal energy at room temperature ($k_B T = 25$ meV) is

often sufficient to dissociate them [29]. However, in organic materials, excitons remain strongly bound due to the low dielectric constant. This strong Coulombic binding significantly affects the charge generation process, as additional energy or a driving force is required to dissociate excitons into free charges. This behavior is closely related to differences in material properties. For instance, the dielectric constant⁴ (ϵ_r) of common inorganic semiconductors such as silicon, germanium, and gallium arsenide ranges from approximately 10 to 12 [30]. In contrast, organic semiconductors have a dielectric constant of about $\epsilon_r \approx 3$ to 4 [31], resulting in a weaker screening of Coulombic interactions. The first organic solar cells (see section 1), characterized by a single-layer, sandwiched configuration, relied on the difference in work functions of the two electrodes for the exciton dissociation. However, the driving force was insufficient, resulting in very low-efficiency devices (<1%).

To overcome this problem, Tang [11] proposed in 1986 a two-layer organic solar cell consisting of a planar heterojunction of donor and acceptor materials. The effectiveness of the exciton dissociation at the donor/acceptor interface in the active layer was associated with a high built-in field of unknown origin. Subsequent studies revealed that an energetic offset between the donor and acceptor LUMO levels plays a crucial role in facilitating exciton dissociation [32]. However, this offset must be carefully balanced, as an excessive LUMO offset leads to energy losses and reduces the open circuit voltage (V_{oc}). At the time, an optimal LUMO offset was proposed to balance exciton dissociation efficiency and minimize V_{oc} loss.

Despite the improved exciton dissociation, the efficiencies of early bilayer OSCs remained limited by several factors, including short exciton diffusion length, the restricted interfacial area for exciton dissociation, and recombination losses. While charges were effectively separated at the interface, the long path to the respective electrodes resulted in high recombination rates. This limitation was addressed more effectively later by the introduction of the bulk heterojunction (BHJ) concept,

⁴ Dielectric constant measures how easily charges are displaced in a material in response to an electric field.

where the donor and acceptor are distributed throughout the active layer, reducing the distance that charges must travel to reach the electrodes.

The development of blending techniques further enabled the processing of the active layer from a single solution containing both donor and acceptor materials. This not only simplified the fabrication process but also facilitated the formation of the interpenetrating networks necessary for efficient charge generation and transport. The ideal morphology and its role in fabricating an efficient device will be discussed in the following section 2.3.

Figure 3.a shows the structure of a conventional OSC, which is composed of an active layer sandwiched by two electrodes. In this layered structure, the current flow is perpendicular to the semiconductor surface. The active layer is the absorbing layer where the photoelectrical process occurs, leading to the generation of charges [33]. The active layer consists of a mixture of at least two types of molecules: one electron-donor and one electron-acceptor. For the anode electrode responsible for the hole collection, a transparent conductive oxide such as indium-tin-oxide (ITO) glass is typically used. The cathode electrode, responsible for the electron collection, should have a low work function to facilitate the electron collection. The simplest option of cathode consists in a calcium layer covered by aluminum. In addition, an electron transport layer (ETL) and a hole transport layer (HTL) are used to selectively extract the free electrons and holes.

Specific focus will now be given to the active layer, composed of two materials with different HOMO and LUMO energies, to discuss the processes involved in charge generation. In donor-acceptor blends, light absorption may occur in either component, giving rise to different photogeneration pathways. As shown in Figure 3, the charge generation process can be described in terms of three main steps [9].

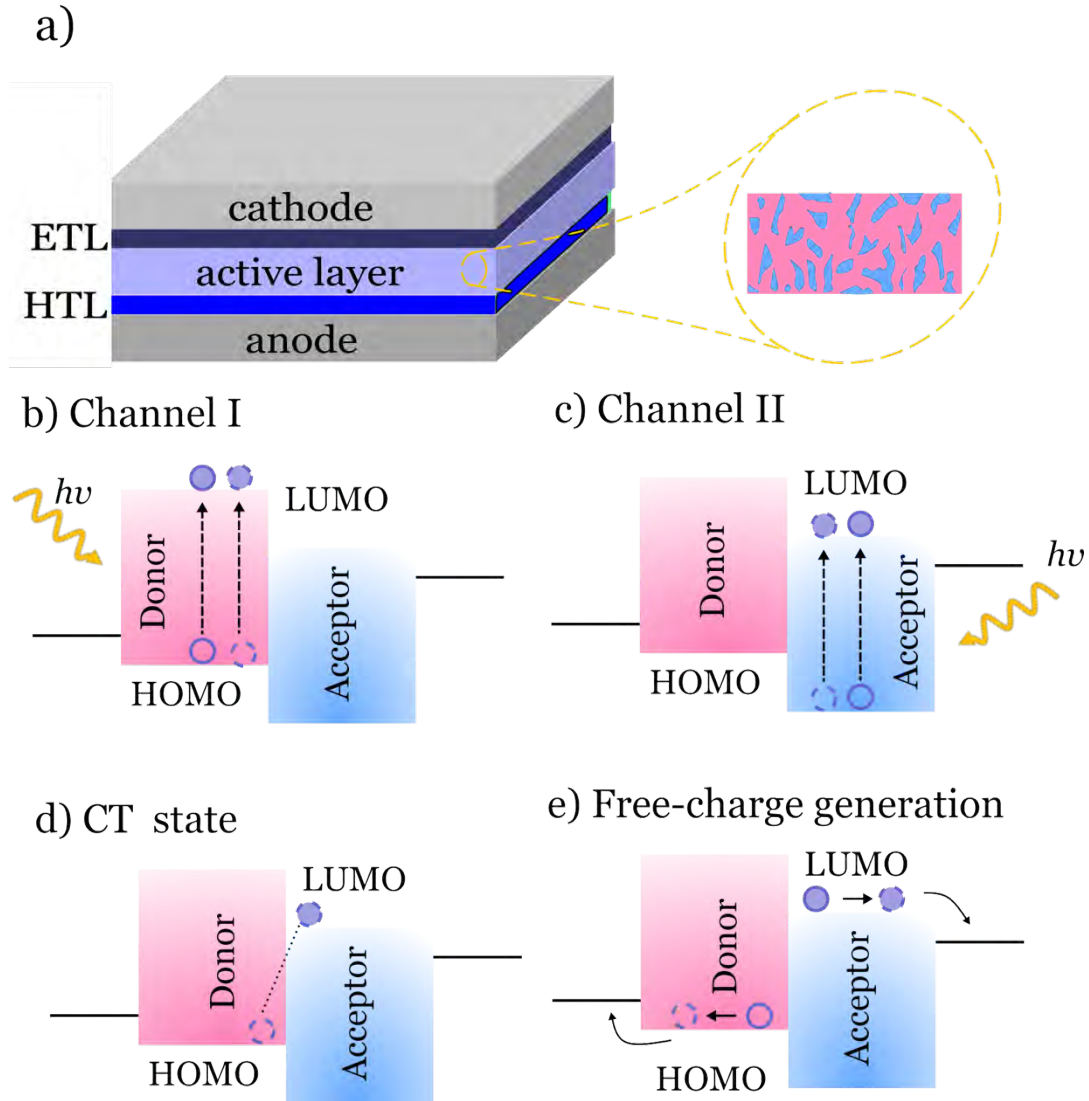


Figure 3. Schematic diagram of a conventional OSC structure (a). Main steps involved in charge photogeneration: first step, photoexcitation, exciton generation and exciton diffusion, occurring either through Channel I in the donor (b) or Channel II in the acceptor (c); second step, formation of the charge-transfer (CT) state at the donor-acceptor interface (d); and third step, dissociation of the CT state into free charge carriers, followed by charge transport and (e).

In the first step (Figure 3.b and 3.c), photons with energy equal to or greater than the energy gap of the active layer materials are absorbed, generating excitons either in the donor (Channel I) or in the acceptor (Channel II). In Channel I, absorption in the donor promotes an electron from the HOMO to the LUMO of the donor. In Channel II, absorption in the acceptor promotes an electron from the HOMO to the LUMO of the acceptor. In both cases, the generated exciton diffuses toward the donor/acceptor interface. One of the loss channels is

associated with this step, where the electron and hole may recombine before reaching the interface. The exciton diffusion length, which determines how far the exciton can travel before recombination, is typically short. In the literature, the reported exciton diffusion length for organic materials is in the range of 5-10 nm [34]. However, higher diffusion lengths in the range of 20-47 nm have been reported for some of the new non-fullerene acceptors [35-38].

In the second step (Figure 3.d), the exciton is dissociated into free charge carriers. In donor-acceptor blends, this process is enabled by energetic offsets at the interface, which drive charge transfer and help overcome the exciton binding energy. If the exciton is formed on the donor, electron transfer to the acceptor can occur, as shown in Figure 3.d; if it is formed on the acceptor, hole transfer to the donor can take place. In both cases, the electron and hole become spatially separated across the interface but remain Coulombically bound in the CT state. Due to the low dielectric constant in these materials, the exciton binding energy is high. The exciton binding energy of organic semiconductors is in the range of 0.1-1.0 eV [39, 40]. Hence, efficient exciton dissociation in organic semiconductors requires donor-acceptor interfaces that provide sufficient energetic driving force for charge transfer, often assisted by the internal electric field of the device.

Finally, in the third step (Figure 3.e), the CT state is dissociated, and the free electron and hole can drift toward their respective electrodes under the influence of the electric field.

The efficiency of the overall power conversion (PCE) is evaluated from the measurement of the current-voltage (J-V) curve of the device under illumination. Figure 4 shows an illustration of a J-V curve in the dark and under illumination, together with the key photovoltaic parameters: the short-circuit density (J_{SC}), defined as the current density at zero applied voltage; open-circuit voltage (V_{OC}), defined as the voltage at which the current becomes zero; fill factor (FF), defined as the ratio of maximum power delivered by the device and the product ($J_{SC} \cdot V_{OC}$), indicating how efficiently photogenerated charges are extracted; and the maximum output power density (P_{max}). The PCE is calculated as the ratio between P_{max} and the power density of incident light (P_{in}):

$$PCE = \frac{P_{max}}{P_{in}} = \frac{(J_{sc} \cdot V_{oc} \cdot FF)}{P_{in}}$$

The shape of the J-V curve reflects the combined effects of charge generation, recombination, transport, and extraction processes described above.

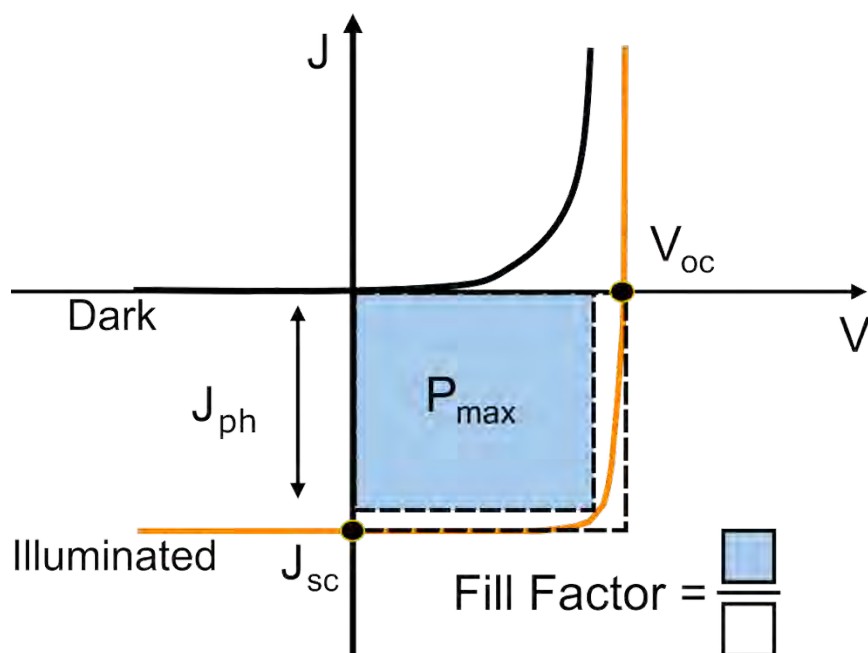


Figure 4. Representation of the solar cell J-V characteristics in the dark and under illumination.

2.3 Morphology of the photoactive layer

In the previous section, the working mechanism of a conventional OSC, specifically the BHJ cell, was discussed. This structure addresses key challenges observed in early organic photovoltaic devices, including the low dielectric constant of organic semiconductors, the limited donor-acceptor interfacial area, and the short exciton diffusion length. By replacing the bilayer structure with an interpenetrating donor-acceptor network, the BHJ provides a large interfacial area for exciton dissociation. However, device performance is not determined by charge generation alone. In organic semiconductors, charge transport is often described in terms of hopping between localized states, particularly in disordered materials, whereas more ordered systems can exhibit more delocalized, band-like transport [41]. Therefore, the morphology of the

photoactive layer plays a central role in both charge generation and charge transport.

The concept of BHJ was first proposed by Heeger et al.[42]. In their work, they propose that an interpenetrating, phase-separated donor-acceptor network would be ideal. By controlling the morphology of this bicontinuous network, a large interfacial area could be achieved throughout the entire active layer, thereby facilitating the exciton dissociation and charge generation. However, in the conventional BHJs processed from D-A solutions, the spontaneously formed domains do not exhibit pure phases. Figure 5 shows a comparison between a conventional and an ideal BHJ. In the ideal device structure, as described by McGehee et al. [43] donor and acceptor pure domains have a width comparable to the exciton diffusion length, with straight pathways to the respective electrodes. Nonetheless, this morphology does not form spontaneously.

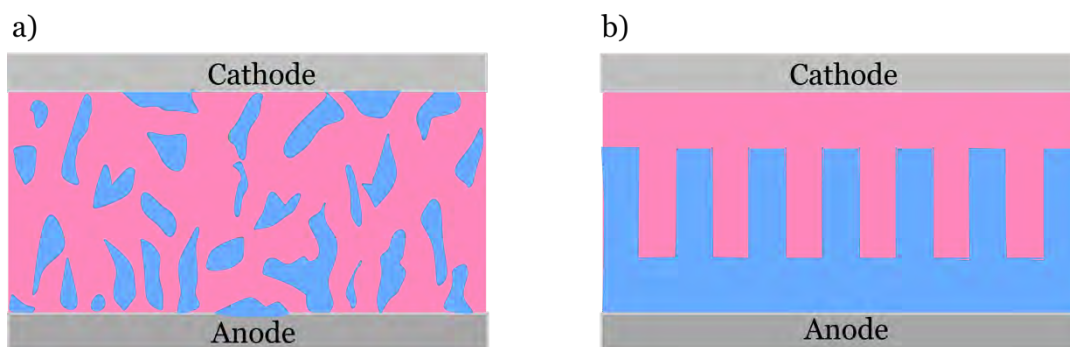


Figure 5. Examples of a) conventional BHJ and b) ideal or ordered BHJ.

In solution-processed OSCs, a blend solution of donor and acceptor materials, usually in a common solvent, is used to fabricate the BHJ. This processing relies on the spontaneous phase separation of the donor and acceptor as the solvent is extracted, which is driven by their interaction energies. The phase separation process will be discussed in the next section. McDowell et al. [44], proposed a route for the solution-processed BHJ formation which can be described in four steps:

1. Solution deposition: the blend solution is deposited onto the substrate.

2. **Surface flow:** in this stage, there is a change in solution concentration or component mixing. For instance, during solvent evaporation, if spin-coating is used, the solution is slung off from the substrate. Consequently, an increase in viscosity and a decrease in material is observed.
3. **Drying:** further evaporation of the solvent occurs followed by the organization of donor and acceptor materials.
4. **Phase separation:** domains that are donor-rich or acceptor-rich are formed.

The morphology of the active layer is influenced by the molecular properties of the donor and acceptor, such as solubility, crystallinity, and molecular weight [45]. In addition to these intrinsic donor/acceptor properties, the morphology is significantly affected by the processing parameters, including solvent choice, temperature, blend ratio, deposition method, substrate, and pre-and post-treatment [46-49].

2.3.1 Sequential deposition

Previously, blending was introduced as a possible method for optimizing the morphology of the active layer by controlling phase separation and, consequently, improving charge transport. On the one hand, blending is a one-step method for obtaining specific structural and physical properties of the molecular mixture in the solid state without the need to synthesize new materials [50]. On the other hand, the morphology depends on various intrinsic parameters and controlling them to achieve a structure closer to the ideal BHJ morphology (Figure 5.b) is not straightforward.

Aiming for the ideal heterojunction, researchers have been exploring the sequential deposition (SD) method for active layer processing. SD involves depositing the donor solution and the acceptor solution sequentially to construct a p-i-n-like structure. The concept of p-i-n structure is to form an active layer that is formed of full layers pure in donor and acceptor near the electrodes, and a region with interpenetrated acceptor and donor in the middle of the film. In principle, the acceptor is cast onto the dry donor layer, or vice versa, depending on

whether the device follows a conventional or inverted architecture. Depending on the choice of solvent, the underlying layer can swell upon contact with the acceptor solution, allowing a limited diffusion of the layer into the bottom layer. According to Li et al. [51] and Jing et al. [52], this method has some advantages over the blending method, namely:

1. The optimization of the solution and film processing is possible for each component (donor and acceptor) separately.
2. Limitations associated with intrinsic properties, including solubility, crystallinity, and miscibility become easier to overcome.
3. The SD appears more suitable for large-area device fabrication.

Recent studies have shown promising results of devices prepared by the SD method, and assigned them to the aforementioned advantages [53-56]. While blending remains a widely used and effective method for active layer optimization, the SD approach offers an alternative strategy with unique advantages. Sun et al. [54] used a polymer donor (P12) characterized by the well-defined fibril morphology, and Y6 to process a p-i-n like structure. P12 was processed from a chlorobenzene (CB) solution, and Y6 processed from a chloroform (CF) solution, was deposited subsequently. The resulting SD device exhibited a PCE of 16.5 %, outperforming the conventional BHJ device, with a PCE of 15%. Additionally, they found that the SD device was insensitive to the polymer's molecular weight (in the range $M_n = 45, 57$ and 91 kg mol^{-1}). Song et al. [53]. reported that the SD method improves the average visible transmittance (AVT) compared to conventional BHJ devices. The optimization of AVT is crucial for semitransparent solar cells. Their strategy was to optimize the donor-acceptor content to reduce the light absorption in the visible range of the spectrum, thereby increasing the device's transparency. Zhan et al. [56] took advantage of the poor miscibility between the donor (PM6) and the acceptor (BTP-S2) to process an active layer with the desired vertical composition distribution. They blended the host acceptor (BO-4Cl) with BTP-S2. The SD-processed ternary device with a BO-4Cl: BTP-S2 blend layer spin-coated over the PM6 layer exhibited a high PCE of 18.16% which exceeded that of SD (17.11%) and BHJ (16.64%) processed ternary devices. Liu et al. [55] used the fullerene derivative indene-C₆₀ bisadduct as the third

component to achieve the desired pseudo-bilayer in PM6/IT-4F devices. This optimized the degree of molecular ordering of PM6, resulting in a 1.05 cm² SD device with a PCE of 14.25%, compared to 13.75% for the corresponding BHJ device. The devices, produced by blade coating, can be scaled up for large area and roll-to-roll processing. Therefore, the combination of better morphology control and scalability makes the SD method an interesting choice.

2.3.2 Thermodynamic aspects of phase separation in polymer blends

As discussed in the previous section, the BHJ morphology plays an important role in the device's working mechanism. Therefore, morphology control is essential for achieving higher efficiency and reproducible device performance. When working with polymer-polymer and polymer-small molecules blends, they can be homogeneous (miscible) or heterogeneous (immiscible). The miscibility of the components is influenced by thermodynamic interactions not only between the solutes themselves, but also with the solvent used during processing [45]. In addition, the rapid solvent evaporation and non-equilibrium nature of spin-coating significantly affect phase separation and thus the final morphology.

The Gibbs free energy of mixing ΔG_m determines whether blending two or more materials is thermodynamically stable as a homogeneous mixture or tends to phase separate [24]. It describes the change in free energy upon mixing and is expressed as:

$$\Delta G_m = \Delta H_m - T\Delta S_m, \quad (1)$$

where T is the absolute temperature, ΔH_m is the change in enthalpy upon mixing, and ΔS_m is the entropy of mixing. ΔH_m represents the variation in interaction energies between molecular surfaces (hydrogen bonds, van der Waals bonds, ions) during the mixing process [57]. ΔS_m denotes the change in entropy due to the rearrangement of molecular species during mixing. The entropy of the system is dependent on the size of the molecular species. For instance, in a polymer-solvent blend

with a high molecular weight polymer, the entropy of mixing is small because of the restricted number of possible molecular configurations (see Figure 6). The sign of ΔG_m determines the spontaneity of the mixing process:

- Negative ΔG_m : mixing is spontaneous, the materials will mix and form a homogeneous solution.
- Positive ΔG_m : mixing is non-spontaneous, and the components are prone to phase separation.

In the case of polymer blends phase separation is likely to occur, because when mixed they do not gain enough entropy to yield a negative ΔG_m [50].

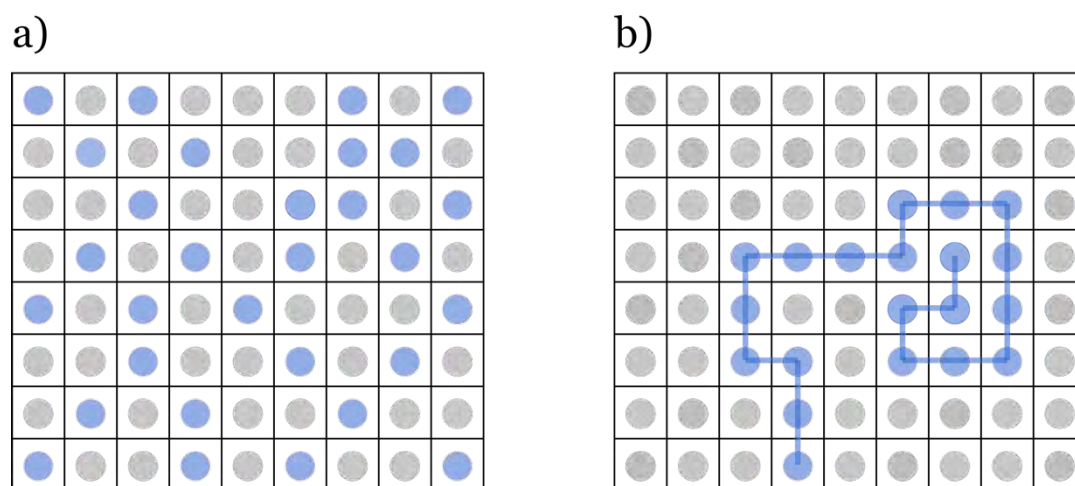


Figure 6. Schematic representation of quasicrystalline lattice model for solutions. a) Mixture of molecules of the same size represented by blue and grey circles. b) Polymer solution, where grey circles represent solvent molecules, and the blue chain represents a polymer molecule.

The relation presented in Equation 1 works well for the simple case of small molecules in solution. However, in the case of polymer systems, modifications are necessary to account the variation in entropy more accurately. In the case of a binary polymer solution, consisting of one polymer and one solvent, the Flory-Huggins theory is often applied. Flory-Huggins theory uses a pseudolattice model to describe the system, where each lattice cell is occupied by either a solvent molecule or a chain segment as indicated in Figure 6.b [57]. Based on this

pseudolattice model the Flory-Huggins equation for the Gibbs free energy of a binary system is:

$$\Delta G_m = RT \left[\frac{\phi_1}{r_1} \ln \phi_1 + \frac{\phi_2}{r_2} \ln \phi_2 + \chi \phi_1 \phi_2 \right] \quad (2)$$

Where R is the ideal gas constant, T is the absolute temperature, ϕ_1 and ϕ_2 are the volume fractions of the solvent (components 1) and polymer (component 2), respectively, r_2 represent the number of polymer segments, and χ is the Flory-Huggins interaction parameter. In the context of a polymer solution, χ account for the interactions between the solvent molecules and the polymer chain segments and can be expressed as:

$$\chi_{12} = \frac{z \Delta \omega_{12}}{\kappa_B T} \quad (3)$$

Where z is the coordination number of the lattice, κ_B is Boltzmann's constant, and $\Delta \omega_{12}$ the interchange energy associated with polymer-solvent interaction. In the Flory-Huggins equation, the first two terms correspond to ΔS_m , and the last term represents ΔH_m .

As shown in Equation 2, the Flory-Huggins theory accounts for the size difference between polymer and solvent molecules and considers the interactions between polymer and solvent, influencing the enthalpy of mixing described by the interaction parameter χ .

The blends used to process a BHJ are usually ternary systems, consisting of donor, acceptor, and solvent. As the solvent evaporates during film formation, the system evolves toward a binary donor-acceptor blend. However, some residual solvent may remain in the final film. For that, ΔG_m is generalized as follows:

$$\Delta G_m = RT \left[\frac{\phi_1}{r_1} \ln \phi_1 + \frac{\phi_2}{r_2} \ln \phi_2 + \frac{\phi_3}{r_3} \ln \phi_3 + \chi_{12} \phi_1 \phi_2 \right. \\ \left. + \chi_{13} \phi_1 \phi_3 + \chi_{23} \phi_2 \phi_3 \right] \quad (4)$$

Using these equations, it is possible to calculate the Gibbs free energy of mixing for all possible compositions of the mixture of interest. This information can be represented as a phase diagram, as shown in Figure 7. It allows for predicting the values of temperature, pressure, and composition at which the mixture will form a single phase or undergo phase separation.

Figure 7.a shows a general phase diagram (temperature versus composition) for a binary system. Figure 7.b shows a general phase diagram for a ternary system, typically presented by an equilateral triangle for a single temperature. The temperature dependence can be depicted by adding a third-dimension axis. The regions where phase separation is possible are delimited by two lines: the binodal (solid line) and the spinodal (dashed line) [58].

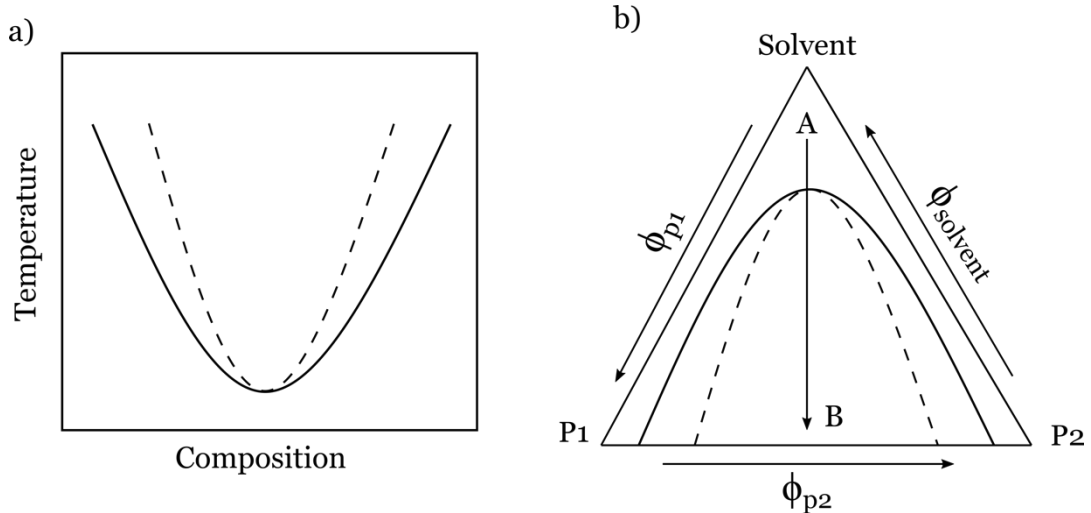


Figure 7. Examples of general phase diagrams for a) a binary system and b) a ternary system, for example, a mixture of solvent and two polymers (P_1 and P_2). The solid line (binodal) defines the boundary between stable and metastable compositions. The dashed line (spinodal) defines the boundary between metastable and unstable compositions. In b) the arrow shows that as the solvent is removed, the mixture becomes less miscible and undergoes phase separation when going from point A (1 phase) to point B (2 phases). Adapted from reference [58].

The phase diagram in Figure 7.b illustrates that the components in the mixture can phase-separate via two different mechanisms: nucleation and growth, and spinodal decomposition [59]. Nucleation and growth occur in the metastable region, defined as the region between the spinodal and binodal lines, while spinodal decomposition occurs in the unstable region, i.e. the region surrounded by the spinodal line. These

two phase separation mechanisms can lead to distinct morphological evolution during phase separation. Examples of morphology often associated with these mechanisms are shown in Figure 8.

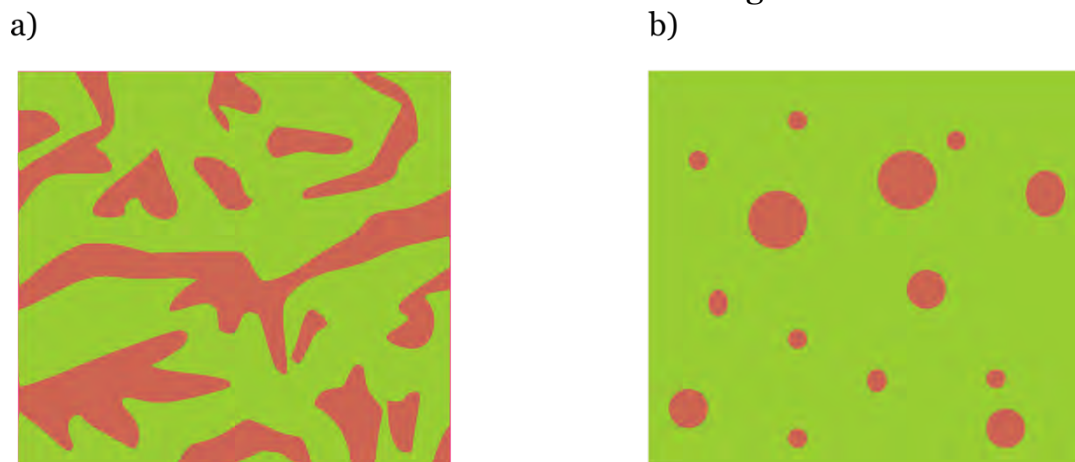


Figure 8. Illustration of morphologies commonly associated with a) spinodal decomposition and b) nucleation and growth. Adapted from reference [59]

2.3.3 Molecular Orientation in Conjugated Organic Semiconductor Films

The morphology resulting from phase separation defines the donor-acceptor network, both laterally and vertically throughout the film. However, the performance of organic solar cells is also strongly influenced by the vertical alignment of the conjugated backbones within these domains. In particular, molecular orientation affects the key processes discussed in Section 2.2, including light absorption, charge separation at the donor-acceptor interface, charge transport toward the electrodes, and extraction by their respective electrodes [60]. Therefore, molecular orientation is an important structural parameter that must be considered alongside phase separation.

Conjugated polymers and small molecules can adopt preferential orientations with respect to the substrate, commonly classified as face-on or edge-on configurations, as illustrated in Figure 9. In a face-on orientation, the conjugated backbone lies parallel to the substrate, whereas in an edge-on orientation, the backbone is oriented perpendicular to the substrate.

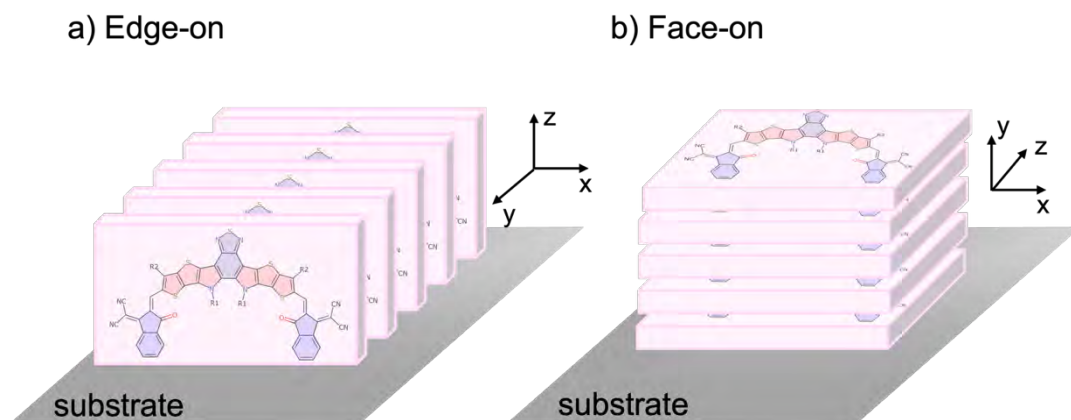


Figure 9. Schematic illustration of molecular orientation of Y5 molecules with respect to the substrate surface: a) edge-on configuration, where the conjugated backbone is oriented perpendicular to the substrate, and b) face-on configuration, where the backbone lies parallel to the substrate. Adapted from reference [61].

In conjugated materials, adjacent molecules can interact through intermolecular $\pi - \pi$ stacking [62], resulting in characteristic stacking distances typically on the order of $\sim 3.3\text{-}3.8 \text{ \AA}$ [63]. For the materials used in this thesis, GIWAXS data have been reported in the literature, $\pi - \pi$ stacking distances extracted from GIWAXS are typically in the range of about $3.6\text{-}3.8 \text{ \AA}$ [64-66]. These interactions enhance intermolecular coupling and influence charge carrier mobility [67]. Since electronic coupling is strongest along the $\pi - \pi$ stacking direction, the molecular orientation with respect to the substrate determines whether efficient transport pathways are aligned parallel or perpendicular to the electrodes. For instance, in conventional solar cell architectures, a face-on configuration promotes $\pi - \pi$ stacking perpendicular to the substrate, which favors vertical charge transport. Similarly, in vertical organic field-effect transistor architectures, a face-on orientation may be more favorable. In lateral field-effect transistors, however, an edge-on orientation is generally more favorable because charge transport occurs parallel to the substrate [68].

In addition to charge transport, molecular orientation can give rise to orientation-dependent surface dipole and quadrupole moments, resulting in measurable shifts in the HOMO and LUMO levels [69]. These shifts can modify both the energy level alignment between the active layer and the electrodes and, in some cases, the relative energy offsets at donor-acceptor interfaces, thereby influencing charge separation

and extraction. Furthermore, molecular orientation influences the anisotropic optical response of conjugated materials [70]. The strength of optical absorption depends on the orientation of the electric field vector of the incident light with respect to the transition dipole moment. Although sunlight is unpolarized, the intrinsic optical anisotropy of the material remains relevant for understanding its spectroscopic response and orientation-dependent measurements.

Molecular orientation is sensitive to processing conditions and interfacial properties. Parameters such as solvent choice, drying kinetics, thermal annealing, and the use of processing additives can significantly influence how molecules organize during film formation [71]. For example, molecular organization is frequently linked to drying dynamics, with high-boiling-point solvents or additives often reported to promote ordering by slowing film formation. However, this effect is not universal, and the resulting orientation depends on the solute-solvent interaction in solution, as it can lead to pre-aggregation. In such cases, solute-solute interaction may dominate over the solute-substrate interaction during the deposition process [72]. Furthermore, the surface energy of the underlying substrate of interfacial layers plays a crucial role in determining preferential orientation, as it governs the interaction between the first molecular layers and the surface [48]. Therefore, controlling molecular orientation involves a complex interplay between different processing conditions and interfacial properties.

3 Materials and sample preparation

In this thesis, the organic semiconductors that were used are:

- Polymer donor PBDB-T: poly[(2,6-(4,8-bis(5-(2-ethylhexyl)thiophen-2-yl)-benzo[1,2-b:4,5-b']dithiophene))-alt-(5,5-(1',3'-di-2-thienyl-5',7'-bis(2-ethylhexyl)benzo[1',2'-c:4',5'-c']dithiophene-4,8-dione)]
- Polymer donor PM6 (fluorinated version of PBDB-T): Poly[(2,6-(4,8-bis(5-(2-ethylhexyl)-4-fluorothiophen-2-yl)-benzo[1,2-b:4,5-b']dithiophene))-alt-(5,5-(1',3'-di-2-thienyl-5',7'-bis(2-ethylhexyl)benzo[1',2'-c:4',5'-c']dithiophene-4,8-dione))]
- Small molecule acceptor Y5: (2,2'-((2Z,2'Z)-((12,13-bis(2-ethylhexyl)-3,9-di-undecyl-12,13-dihydro[1,2,5]thiadiazolo[3,4e] thieno[2'',3'':4',5'] thieno[2',3':4,5]pyrrolo[3,2-g] thieno[2',3':4,5] thieno[3,2-b]-indole-2,10-diyl)bis(methanylylidene)) bis(3-oxo-2,3-dihydro-1H-indene-2,1-diylidene))dimalononitrile)]
- Small molecule acceptor Y6 (fluorinated version of Y5): 2,20-((2Z,20Z)-((12,13-bis(2-ethylhexyl)-3,9-diundecyl-12,13-dihydro-[1,2,5] thiadiazolo[3,4-e]thieno[2,30':4',50] thieno[20,30:4,5]pyrrolo[3,2-g] thieno[20,30:4,5]thieno[3,2-b]indole-2,10-diyl)bis(methanylylidene)) bis(5,6-difluoro-3-oxo-2,3-dihydro-1H-indene-2,1-diylidene))dimalononitrile)]
- Polymer acceptor PF5-Y5: Poly[(2,2'-((2Z,2'Z)-((12,13-bis(2-ethylhexyl)-3,9-diundecyl-12,13-dihydro[1,2,5]thiadiazolo[3,4e]thieno[2'',3'':4',5']thieno[2',3':4,5]pyrrolo[3,2-g]thieno[2',3':4,5]thieno[3,2-b]-indole-2,10-diyl)bis(methanylylidene))bis(3-oxo-2,3-dihydro-1H-indene-2,1-diylidene))dimalononitrile-alt-2,6-(4,8-bis(5-(2-ethylhexyl)-3-hexyl)thiophen-2-yl)-benzo[1,2-b:4,5-b']dithiophene))]
- Polymer acceptor PYT: (Poly[(2,2'-((2Z,2'Z)-((12,13-bis(2-octyldodecyl)-3,9-diundecyl-12,13-dihydro[1,2,5]thiadiazolo[3,4e]thieno[2'',3'':4',5']thieno[2',3':4,5]pyrrolo[3,2-

g]thieno[2',3':4,5]thieno[3,2-b]-indole-2,10-diyl)bis(methanylylidene))bis(3-oxo-2,3-dihydro-1H-indene-2,1-diyliidene)) di-malononitrile-alt-2,5-thiophene))

3.1 Polymer donor PBDB-T and PM6

PBDB-T (Figure 10.a) is a donor alternating copolymer composed of donor-acceptor (D-A) repeating units. The donor moiety (BDT-T), shown in pink, consists of a benzodithiophene (BDT) core and thiophene side chains. The acceptor moiety (BDD), shown in purple, consists of a benzodithiophene-4,8-dione unit functionalized with carbonyl and thiophene side chains.

First synthesized by Qian et al. [73], PBDB-T achieved a PCE of 6.67% when combined with the fullerene acceptor PC61BM. In the literature, alternative names for PBDB-T include PD1, PBDBTBD, and PCE12 [74].

PBDB-T has an optical gap of 1.8 eV. It exhibits an impressive absorption coefficient, temperature-dependent absorption spectra, a deep-lying HOMO level, and high carrier mobility [73]. Moreover, systematic studies on temperature-dependent absorption spectra reveal that PBDB-T's strong tendency to aggregate in solution provides a practical approach to modulating domain size without changing crystallinity, thereby enabling the achievement of an optimized morphology.

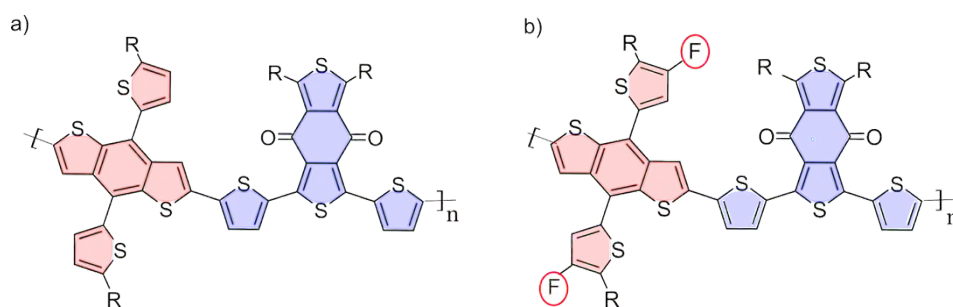


Figure 10. Molecular structure of a) PBDB-T and b) PM6, where R = 2-ethylhexyl.

Aiming for a better energy alignment with the fluorinated acceptor, Jianhui Hou's group optimized PBDB-T by the introduction of fluorine

and alkylthiol substituents to the conjugated thiophene side groups [75]. The resulting polymer donor derivative PM6 (Figure 10.b) exhibits a similar optical gap (≈ 1.8 eV) and a deeper HOMO level of -5.45 eV as compared to PBDB-T (-5.28 eV). Similar to PBDB-T, it presents a strong tendency to aggregate in solution and in the solid state, pronounced $\pi - \pi$ stacking, and fibrillar morphology.

PM6 combined with the small molecule acceptor Y6 became one of the benchmark systems in high efficiency non-fullerene organic solar cells [76-78]. The PM6:Y6 system played a central role in pushing single-junction organic photovoltaics beyond 15 % efficiency and established material design principles that were later adopted in next-generation donor-acceptor systems, which eventually achieved efficiencies above 20 % [79].

3.2 Small molecules Y5 and Y6

Y5 and Y6 are molecular electron-acceptors, often called small molecule acceptors (SMAs). They have a planar structure composed of conjugated fused rings [76, 80]. The conjugated structures shown in Figure 11 are composed of A-D-A'-D-A repeating units. This structure stems from the earlier A-D-A type of SMAs by replacing the core donor unit (D) in A-D-A type SMAs with a more extended fused central unit [81]. These SMAs are members of the so-called Y-series, first synthesized by Yuan et al. [82], and include benzothiadiazole (BT) as an electron-deficient unit in the central fused ring.

Y6, a fluorinated derivative of Y5, was developed by introducing fluorinated end groups. This modification aimed to enhance absorption and promote intermolecular interactions by forming non-covalent F...S and F...H bonds, thereby facilitating charge transport. In the literature, alternative names for Y6 include BTP-4F and PCE 157.

OSCs based on A-D-A'-D-A NFAs exhibit relatively higher short-circuit current density (J_{sc}) and fill factor (FF), along with a comparable open-circuit voltage (V_{oc}) [81]. These performance enhancements are attributed to redshifted absorption, favorable nanoscale morphology, and suppressed charge recombination.

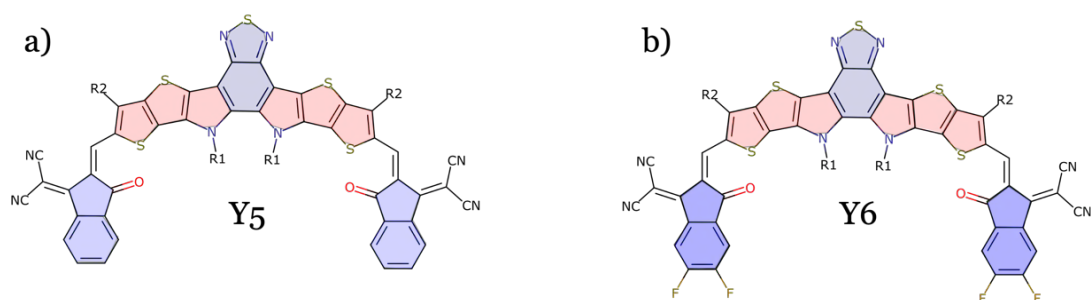


Figure 11. Molecular structures of a) Y5 and b) Y6, where R1 = 2-ethylhexyl and R2 = undecyl.

3.3 Polymer acceptors PF5-Y5 and PYT

To address challenges presented by SMAs such as strong self-aggregation, unsatisfactory mechanical strength, and limited thermal stability, the polymerized small molecules (PSMs) approach has been widely explored. In this thesis, two polymerized small molecules, PF5-Y5 and PYT, have been investigated.

The PF5-Y5 polymer acceptor depicted in Figure 12.a, is a low-bandgap polymer (1.68 eV) first synthesized by Fan et al. [83]. It is an alternating copolymer based on the Y5 SMA. PF5-Y5 consists of alternating Y5 units (highlighted in purple) acceptor units, and BDT-T donor moieties (highlighted in pink). Studies conducted by Fan et al. revealed that the PF5-Y5 neat film exhibits significant improvements in their properties, including absorption coefficient ($\sim 1.45 \cdot 10^5 \text{ cm}^{-1}$), electron mobility ($\sim 3.18 \cdot 10^{-3} \text{ cm}^2 \text{ V}^{-1} \text{ s}^{-1}$), and favorable molecular crystallinity and packing characteristics.

Moreover, the all-polymer solar cells based on PBDB-T: PF5-Y5 show better thermal stability. These devices retained $\sim 75\%$ of their initial PCE after 2500 min of storage at 85°C , whereas devices fabricated with PBDB-T: Y5 blends retained only $\sim 55\%$ of their initial efficiency under the same conditions.

Figure 12.b illustrates the polymer acceptor PYT, first synthesized by Wang et al.[84]. Like PF5-Y5, PYT is an alternating copolymer based on the Y5 SMA; however, in PYT, thiophene is used as the linking unit instead of BDT-T. This polymer acceptor has broad absorption with a narrow bandgap of $\sim 1.40 \text{ eV}$, and a high absorption coefficient $> 1.00 \cdot 10^5 \text{ cm}^{-1}$.

Wang et al. demonstrated that the molecular crystallinity and miscibility of PYT can be fine-tuned by modifying its molecular weight, with minimal impact on its energy levels. They also showed that PYT exhibits good thermal stability: for the low molecular weight variant, only 5% of weight loss was observed at 300°C , and an increase in molecular weight further improved the onset thermal decomposition temperature.

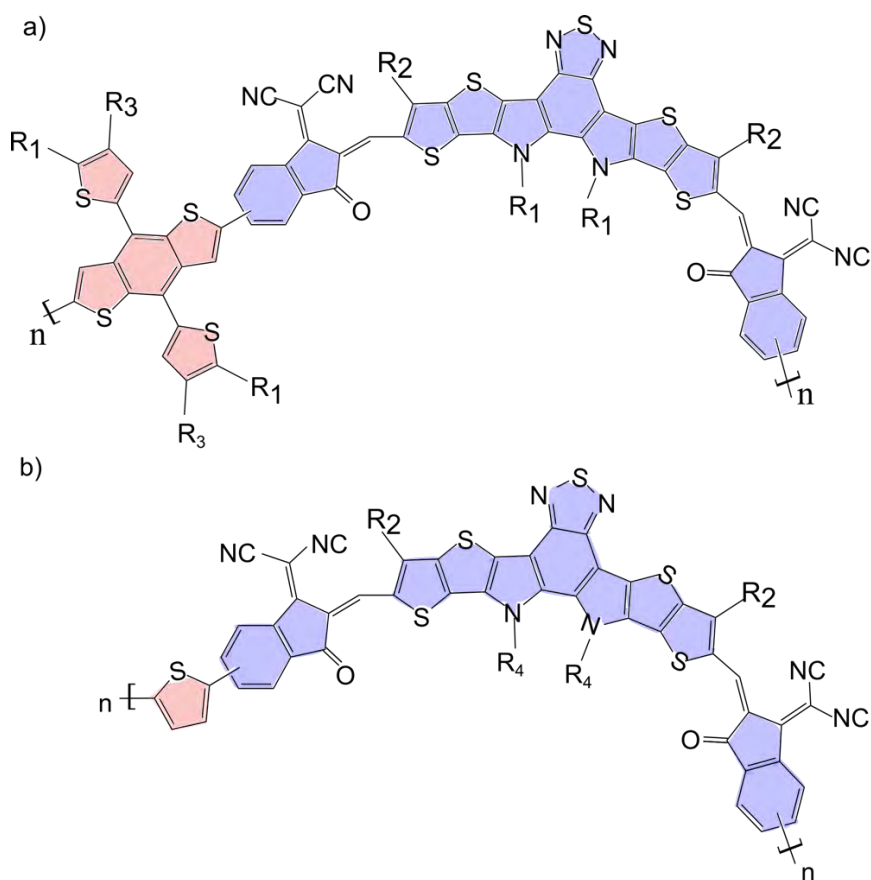


Figure 12. Molecular structures of a) PF5-Y5 and b) PYT, where R_1 = 2-ethylhexyl and R_2 = undecyl, R_3 = hexyl and R_4 = 2-octyldodecyl.

3.4 Sample preparation

3.4.1 Spin-coating for film deposition

Spin-coating is a widely used technique for thin film deposition on small substrates, particularly in fields such as microelectronics, photonics, and biotechnology. This method enables the production of highly uniform thin films with controlled thickness and is therefore widely used in laboratory-scale research. However, because it is mainly suited to small area coating, its application in large-scale industrial manufacturing is limited.

Spin-coating has the advantage of being simple, inexpensive, and versatile. It can be performed under ambient conditions, unlike vacuum-

based deposition techniques such as Physical Vapor Deposition (PVD). However, one limitation of spin-coating is that it is most effective for small substrates, as film homogeneity can become problematic for larger areas.

As a solution-based technique, spin-coating is commonly used to fabricate OSC active layers by depositing a solution containing the organic semiconductor materials onto a substrate. The equipment typically consists of a rotating platform mounted on a motorized axis capable of operating at different speeds. The spin-coating process can be described as a multi-step procedure consisting of four stages, as illustrated in Figure 13.

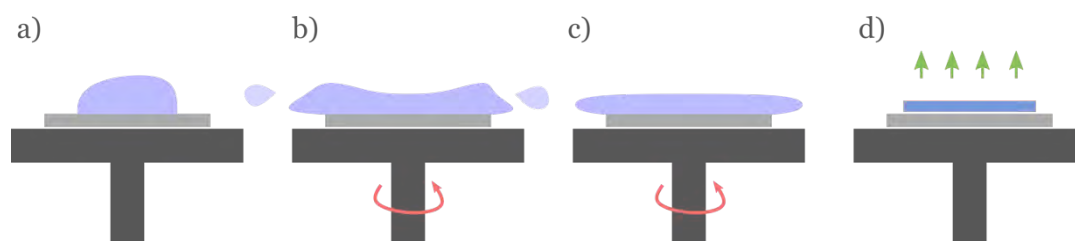


Figure 13. Schematic representation of the spin-coating process steps; a) dispense step, b) spin up step, c) spin off step and d) drying (solvent evaporation).

In the dispensing step (Figure 13.a), a drop of the blend solution is deposited onto the substrate. The amount of solution used will depend on the size of the substrate to be coated. This step can be performed with the substrate motionless (static dispense) or with the substrate spinning at low speed (dynamical dispense). Dynamic dispense is usually preferred over static dispense because it allows the solution to spread over the whole substrate and offers more control over the process. For instance, this becomes crucial when working with volatile solvents, such as chloroform; in the dynamic mode, the solvent has less time to evaporate before the start of the spinning.

In the subsequent step (Figure 13.b), the substrate is accelerated until it reaches the desired rotation speed, typically in the range of 500-4000 rpm. During the acceleration, the solution is spread across the substrate, and excess solution is expelled from the substrate surface. Initially, due to the fluid's thickness and inertia, it does not rotate at the

same speed as the substrate [85]. After a short time, the fluid film becomes thin enough to co-rotate with the substrate.

In the third step (Figure 13.c), the substrate rotates at a constant speed. As further solvent evaporation occurs, the viscosity of the film increases, leading to the formation of a uniform thin film [86]. At this stage, the flow is increasingly governed by viscous force, as the rising viscosity resists further redistribution of the liquid across the substrate. In the fourth step (Figure 13.d), the expulsion of fluid stops, and the thinning of the film is dominated by evaporation of the solvent. The film drying time depends on the evaporation rate of the solvent, which is determined by its properties, including boiling point, vapour pressure, and ambient conditions.

In general, the final film thickness is proportional to the inverse of the square root of spin speed as shown in Equation 5 [87].

$$h_f \propto \frac{1}{\sqrt{\omega}} \quad (5)$$

The $\omega^{-\frac{1}{2}}$ dependence may vary due to the influence of factors such as material concentration and the properties of the solvent.

4 Characterization Techniques

4.1 Atomic force microscopy

Atomic force microscopy (AFM) is a powerful surface characterization technique in the scanning probe microscopy family. It was proposed by Binnig and Quate in 1986, as a combination of the principles of the scanning tunneling microscope (STM) and the stylus profilometer, capable of measuring forces as small as 10^{-8} N [88]. The AFM is based on the measurement of forces between a sharp probe and a sample surface. The forces can be classified as chemical forces (short range), van der Waals and electrostatic forces (long range), capillary forces (in air), and magnetic forces [89]. The tip-sample interaction can be qualitatively discussed using a model potential, such as the Lennard-Jones potential. In this model, the tip-sample interaction is reduced to a simpler system, consisting of two neutral atoms interacting by a potential composed of contributions of short- and long-range forces. Equation 6 shows the Lennard-Jones potential, where U_0 is the depth of the potential well, d is the distance between the tip and sample, and R_a is the distance at which $U_{LJ}(d)$ is zero [90].

$$U_{LJ} = 4U_0 \left[\left(\frac{R_a}{d} \right)^{12} - \left(\frac{R_a}{d} \right)^6 \right] \quad (6)$$

Figure 14.a shows the attractive (green line) and the repulsive (pink line) contributions to the Lennard-Jones potential, which are proportional to $\frac{1}{d^{12}}$ and $\frac{1}{d^6}$, respectively. Figure 14.b shows the force-distance curve, as a result of the attractive and repulsive contributions of tip-sample interaction. Once the probe is brought closer to the sample, the Van der Waals force rises due to temporary fluctuating dipoles, resulting in an attractive interaction. However, the closer the probe gets to the sample surface, the stronger the repulsive forces get due to the interaction of the electron clouds of the atoms in the probe and in the surface.

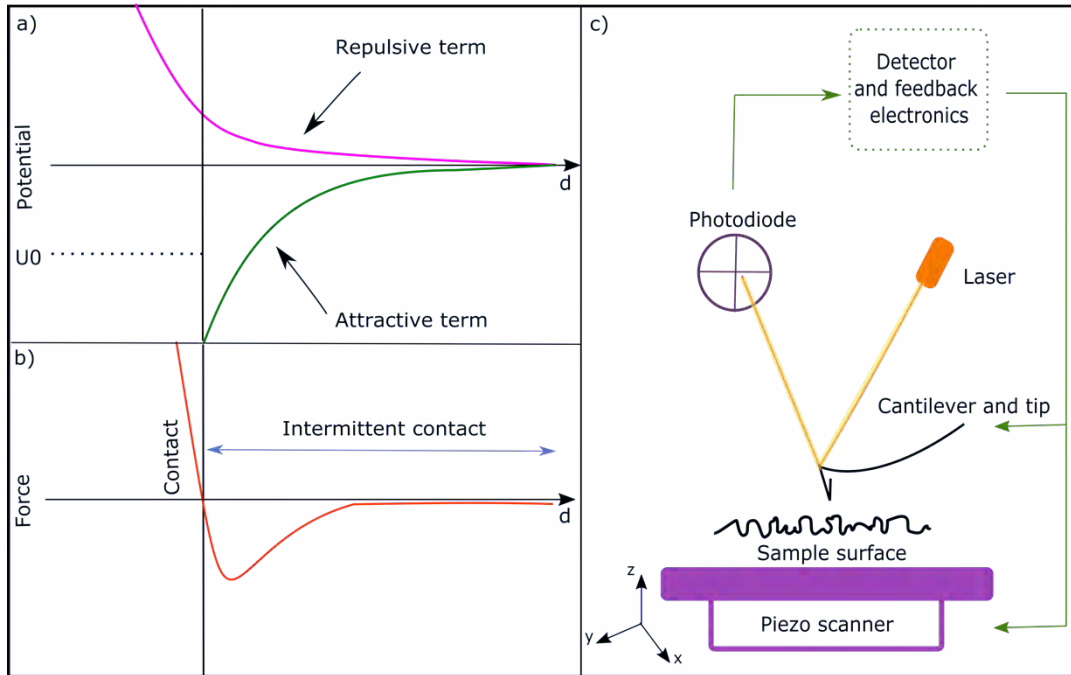


Figure 14. a) Lennard-Jones potential as a function of the tip-sample d . The pink and green curves represent the attractive and repulsive contributions to the potential, respectively (d). b) Force curve showing the contact and intermittent contact working ranges, which determine the AFM operation mode. c) Schematic diagram of the AFM instrument.

The probe is placed on the end of a cantilever, which will experience deflections, depending on the forces involved. Therefore, the cantilever acts as a force sensor during the surface scanning. The cantilever deflections are very small, consequently, an indirect way of detecting it is needed. Deflection sensors can be based on different techniques, such as beam deflection, interferometry, capacitance, piezoresistance, and piezoelectricity [89]. The AFM used in this work is based on the beam-deflection method, i.e., a light beam is reflected off the back side of the cantilever, and the deflection is monitored by a position-sensitive photodiode, as shown in the schematic diagram Figure 14.c. AFM measurements can be performed in different detection working regimes, static or dynamic; within these working regimes, there are different operation modes concerning the tip-sample separation, such as contact, intermittent contact, and non-contact.

Contact mode is the most used among the static modes. In contact mode, the tip is dragged across the surface in contact; the measurement is performed in the repulsive regime (Figure 14.b). The tip-sample distance is controlled through a feedback loop that maintains a constant

cantilever bending [89]. The variation in the vertical movement of the cantilever, referred to as the z-signal, is recorded and presented as a topographic (height) image. However, this mode is challenging when characterizing soft samples, since the direct contact may induce damage to the sample. To overcome this, tapping mode was developed [91].

Tapping mode is a dynamic mode, and it is performed in the intermittent contact regime of the force curve (Figure 14.b). In tapping mode, the cantilever is excited to vibrate at or close to its resonance frequency while it is scanning across the sample surface. As the tip is intermittently touching the surface, it experiences changes in the resonance frequency and consequently in the oscillation amplitude due to the tip-sample force interactions. The amplitude contains information on the average tip-sample distance, d , and therefore, the amplitude is the signal used as a feedback parameter. The z-signal is adjusted to keep a constant oscillation amplitude and recorded as the signal that yields the topography image. Tapping mode is particularly suitable for soft or weakly adhered samples, since it minimizes the risk of sample deformation or delamination during imaging.

4.1.1 PeakForce quantitative nanomechanical mapping

PeakForce quantitative nanomechanical mapping (PF-QNM) is an advanced scanning probe microscopy (SPM) mode based on PeakForce tapping mode. In PeakForce Tapping mode, a force-distance curve is measured at every pixel in the image, and the resulting peak interaction force of each of these force curves is used as imaging feedback signal. This is enabled by the choice of a modulation frequency of about 1 to 2 kHz, which is much lower than the cantilever's resonant frequency [92].

In addition to using the force curve to determine the peak interaction force as the control feedback signal, the software extracts from each force curve the sample's mechanical properties, such as elastic modulus and deformation. The elastic modulus reflects the local stiffness of the material, while the deformation corresponds to the maximum indentation experienced by the surface under the applied PeakForce.

The elastic modulus is obtained by fitting the repulsive (contact) portion of the retract segment of the force-distance curve using the Derjaguin-Muller-Toporov (DMT) contact mechanic's model. This model describes the elastic deformation of a material under a spherical indenter while accounting for adhesive interactions outside the contact area and is appropriate for materials with relatively low adhesion [93, 94]. In the DMT framework, the interaction force F is described by:

$$F - F_{adh} = \frac{4}{3}E^*\sqrt{R}(d - d_0)^{\frac{3}{2}}, \quad (7)$$

where F_{adh} is the adhesion force, R is the tip radius, and $d - d_0$ represents the indentation depth (deformation). The reduced modulus E^* is treated as a fitting parameter and is obtained by fitting the experimental force-indentation curve with the DMT expression. It is related to the Young's modulus of the sample (E_s) and the tip (E_{tip}) through:

$$\frac{1}{E^*} = \frac{1 - \nu_s^2}{E_s} + \frac{1 - \nu_{tip}^2}{E_{tip}} \quad (8)$$

where ν_s and ν_{tip} are the Poisson ratios of the sample and tip, respectively. Since the AFM tip is significantly stiffer than the polymer sample ($E_{tip} \gg E_s$), the tip contribution can be neglected. The modulus values shown in the AFM images are derived from the fitted reduced modulus using the assumptions of the applied DMT model, including an assumed Poisson ratio for the sample.

The local deformation is extracted directly from force-distance curve as the indentation depth at the applied peak force, defined as the difference in the z-position between the point of first tip-sample contact and the tip position at the peak force.

As an example, we show in Figure 15 PF-QNM measurements of a TQ₁:PC₇₀BM blend. In this mode, topography, DMT modulus, and deformation are measured simultaneously. The TQ₁:PC₇₀BM blend is a well-studied system and, under the specific processing condition used here (chlorobenzene as the solvent and a donor-acceptor ratio of 1:3),

exhibits strong phase-separation with large globular domains of approximately 100-300 nm. Compositional study by scanning transmission X-ray microscopy (STXM) and dynamic secondary ion mass spectroscopy (d-SIMS) shows that the globular domains are rich in PC₇₀BM, while they are surrounded by a TQ₁-rich phase. These reports also show the formation of a TQ₁-rich layer at the film surface, attributed to surface energy minimization [95, 96].

The distribution of the DMT modulus values in the scan region shows three peaks, centered at 2.7 GPa, 3.5 GPa, and 5 GPa. The stiffest (brightest) regions arise from PC₇₀BM-rich domains, while the peak at 3.5 GPa corresponds to the TQ₁-rich regions. Consequently, in the deformation image, the lowest deformation is observed for the PC₇₀BM-rich domains. It is important to note that the DMT modulus signal from the PC₇₀BM-rich domains is not homogeneous and shows values of approximately 5-6 GPa, which are lower than that of pure PC₇₀BM (12 GPa), reflecting the presence of TQ₁ in their composition. At the edges of the globular domains, which appear black in the DMT modulus map, artifacts are observed, likely due to altered contact mechanics at the domain boundaries [97].

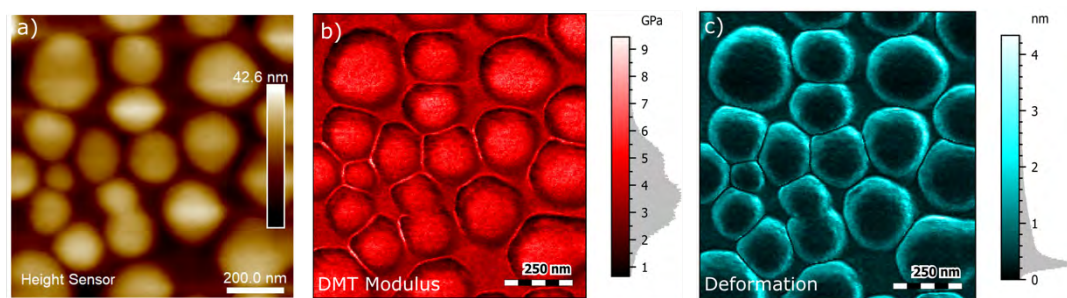


Figure 15. PF-QNM measurements on TQ₁:PC₇₀BM blend prepared in CB with a ratio 1:3. a) Topography, b) DMT modulus, and c) deformation. Measurements were carried out by I. Benamar as part of his Master's thesis [98]. Samples were prepared by the author.

Overall, the TQ₁:PC₇₀BM blend provides a well-defined and phase-separated morphology that serves as a suitable model system for demonstrating AFM-based characterization techniques. Because the PC₇₀BM-rich and TQ₁-rich domains can be clearly distinguished, this system is well-suited not only for nanomechanical characterization but also for probing the additional local properties discussed in the following

sections. Therefore, this system will be used to illustrate the capabilities of additional AFM modes.

It should be noted that the strong phase separation observed in the TQ₁:PC₇₀BM system represents a comparatively simple morphological case. In contrast, modern non-fullerene acceptor systems such as PBDB-T:Y6 typically exhibit a much finer and more intermixed morphology. In such systems, the reduced mechanical contrast between donor- and acceptor-rich regions makes the interpretation of AFM-based nanomechanical mapping more challenging.

4.1.2 Kelvin Probe Force Microscopy

Kelvin Probe Force Microscopy (KPFM) measures the long-range electrostatic interaction between a conductive AFM tip and the sample surface. The technique is based on the (macroscopic) Kelvin probe, an experimental setup introduced by Lord Kelvin in 1898, used to measure the work function difference ($\Delta\phi$) between two metallic electrodes [99]. In the classical Kelvin probe, the distance between the electrodes is periodically varied, which modulates the capacitance of the system. If a contact potential difference (CPD) exists between the electrodes, this time-varying capacitance generates an AC current. A DC bias is then applied to null this current, allowing the work function difference to be determined. In KPFM, the tip and the sample act as the two electrodes, enabling nanoscale mapping of the sample's local surface potential.

The physical origin of the contact potential difference (CPD) is schematically illustrated in Figure 16. When the tip and sample are electrically connected, electrons redistribute until their Fermi levels align. This charge redistribution generates a CPD represented by a relative shift in their vacuum energy levels. The CPD is given by:

$$V_{CPD} = \frac{\Delta\phi}{e} = \frac{\phi_{sample} - \phi_{tip}}{e}, \quad (9)$$

where ϕ is the work function, and e is the elementary charge [100]. In this work, the sample work function is related to the measured CPD via

$$\phi_s = \phi_{tip} + eV_{CPD} \quad (10)$$

Regions that exhibit higher (less negative) V_{CPD} values correspond to a higher sample work function.

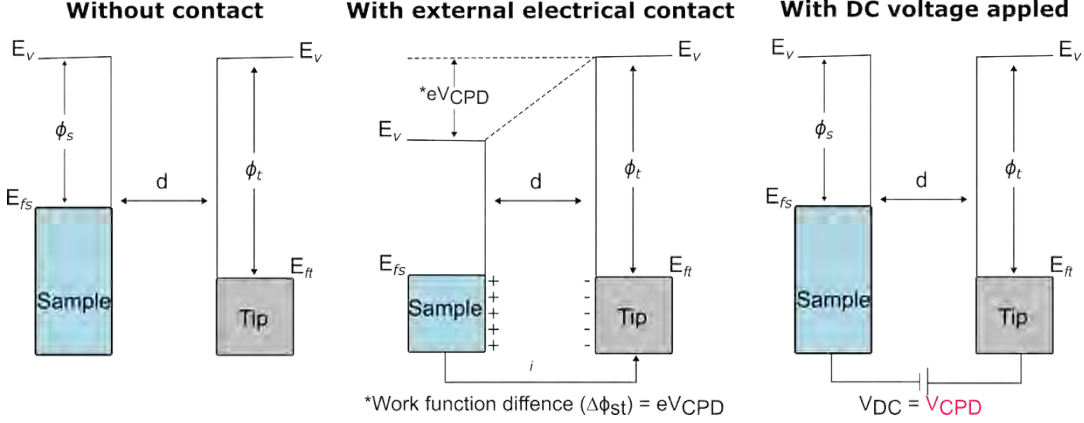


Figure 16. Schematic illustration of the physical mechanism of KPFM. In this case, the tip has a higher work function than the sample. Before electrical contact is established, the vacuum levels of the two materials are aligned, while their Fermi levels differ. Once the electrical contact is made, electrons flow until both tip and sample Fermi levels align. This charge redistribution results in a contact potential difference (CPD) between tip and sample, leading to an offset of their vacuum energy levels.

In heterodyne KPFM mode, an AC voltage (V_{AC}) at frequency ω_1 is applied to the conductive tip in addition to a DC bias (V_{dc}). Simultaneously, the cantilever is mechanically driven near its resonance frequency ω_0 . The electrostatic force between the tip and the sample can be expressed as:

$$F_{elec} = -\frac{1}{2} \frac{\partial C}{\partial z} (V_{DC} + V_{AC} \sin(\omega_1 t) - V_{CPD})^2 \quad (11)$$

where $\frac{\partial C}{\partial z}$ is the capacitance gradient with respect to the tip-sample distance. Because the cantilever is oscillating mechanically while the tip is also electrically modulated, the electrostatic force contains mixed-frequency components arising from frequency mixing between ω_1 and ω_0 . In the heterodyne KPFM, this mixing generates force components at $\omega_1 \pm \omega_0$ [101]. These heterodyne signals are demodulated using a lock-in amplifier, and the DC bias is adjusted via a feedback loop to null the selected mixed-frequency electrostatic force component. Under this

nulling condition, $V_{DC} = V_{CPD}$ and the applied DC voltage directly represents the local surface potential.

In the dark, the measured CPD reflects the local work function difference between the tip and the sample. Under illumination, changes in CPD correspond to the surface photovoltage (SPV), which arises from photoinduced charge separation and the associated splitting of local quasi-Fermi levels in donor-acceptor systems [102, 103].

Figure 17 shows KPFM measurement on TQ₁:PC₇₀BM in dark and under illumination. In the dark, the PCBM-rich domains show a less negative CPD values as compared to the TQ₁-rich matrix, indicating a higher work function of the acceptor-rich regions. Upon illumination, an overall negative shift in V_{CPD} is observed across the film.

This global negative SPV originates from photoinduced charge redistribution in the blend film. Under illumination, this behavior is consistent with electron accumulation in the PC₇₀BM phase near the probed surface and corresponding hole depletion at that surface. Such electron accumulation shifts the electron quasi-Fermi level upward, i.e., toward the vacuum level. Since the work function is defined as $\phi = E_{vac} - E_F$, an upward shift of the quasi-Fermi level reduces the work function [102, 103]. According to $\phi_s = \phi_{tip} + eV_{CPD}$, this reduction in work function results in a negative shift of about 300 mV in V_{CPD} , consistent with the observed overall SPV.

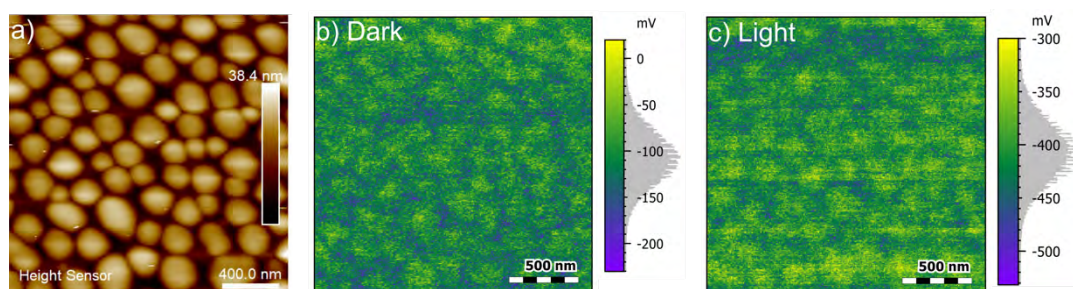


Figure 17. KPFM measurements on TQ₁:PC₇₀BM blend prepared in CB with a ratio 1:3. a) Topography, b) CPD map in dark, and c) CPD map under illumination. Measurements were carried out by I. Benamar as part of his Master's thesis [98]. Samples were prepared by the author.

In summary, KPFM enables spatially resolved mapping of local work function variations and surface photovoltage in donor-acceptor blends.

These measurements provide insight into charge redistribution and quasi-Fermi level shifts at the nanoscale. However, KPFM does not directly probe charge generation. To complement this information with spatially resolved measurements of photocurrent generation and collection, photoconductive atomic force microscopy (pc-AFM) was employed, as described in the following section.

4.1.3 Photoconductive Atomic Force Microscopy

Photoconductive Atomic Force Microscopy (pc-AFM) combines conductive AFM (c-AFM) operated in contact mode with a light source. In c-AFM a conductive probe is used as a nanoelectrode, enabling the spatial mapping of the sample conductive network under applied bias. In addition to current mapping, local current-voltage (I-V) spectroscopy can be performed to characterize the electrical response of the nanoscale tip-sample junction at specific positions.

When a light source is introduced, the technique allows detection of, photogenerated current, providing spatially resolved information about charge generation and charge collection. Depending on the donor-acceptor system and the energy level alignment at the junction, the measured photocurrent can be correlated with either donor- or acceptor-rich domains. Thus, pc-AFM combines spatially resolved photocurrent mapping with local electrical characterization, offering insight into the origin of variations observed in macroscopic device performance.

Once again, we use TQ₁:PC₇₀BM as a model system. Figure 18 depicts the topography image and the photocurrent map taken simultaneously. Due to the higher work function of the PtIr tip compared to ITO, the polarity of the measured current differs from that in an organic solar cell with conventional ITO/HTL/active layer/ETL device architectures. In this configuration, the PtIr tip preferentially collects photogenerated holes (from the TQ₁-rich domains), because the high work function of the PtIr makes hole extraction from the donor more energetically favorable. Photogenerated electrons are preferentially transported through the PC₇₀BM-rich globular domains toward the ITO substrate. Consequently, the photocurrent collected at the tip flows from

the sample toward the tip, opposite to the current direction in standard device architectures.

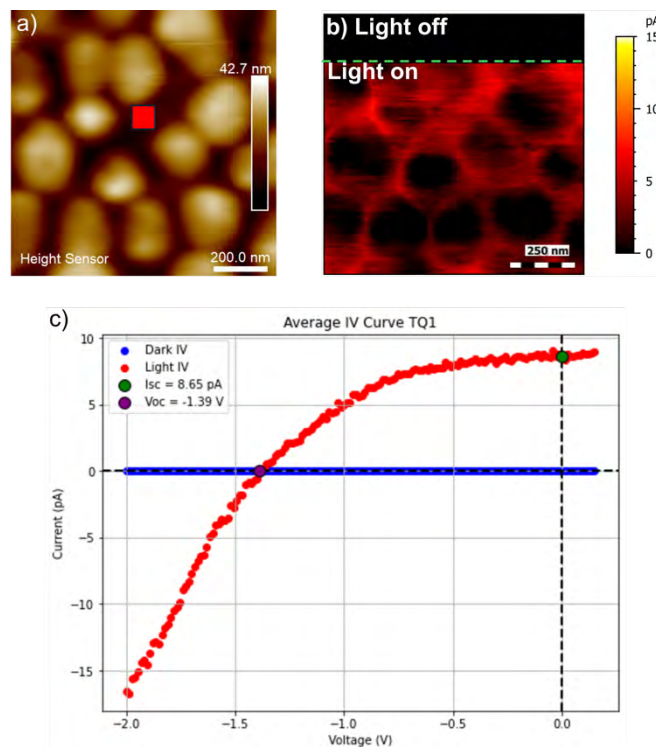


Figure 18. Pc-AFM measurements on TQ₁:PC₇₀BM (1:3) blend prepared from solution in CB. a) contact mode height image. b) current map in dark (top) and under illumination (bottom). c) I-V curves in dark and under AM 1.5 illumination at a TQ₁-rich region. The sample was illuminated through the ITO/glass substrate using a xenon arc lamp-based solar simulator (Newport, model 67005) operated at 80 W, with light delivered via a liquid light guide (Oriel p/n 78254). Measurements were performed under short-circuit conditions using a PtIr-coated probe. Experiments carried out by I. Benamar as part of his Master's thesis [98]; samples were prepared by the author.

No measurable current is detected in the dark, as can be seen at the top of Figure 18.b. Upon illumination, a clear photocurrent signal appears, revealing pronounced contrast. The globular domains appear predominantly dark, indicating negligible photocurrent, while the surrounding matrix exhibits significant photocurrent collection. This contrast is consistent with preferential hole collection by the tip from donor-rich regions. In addition, since TQ₁ is the main light-absorbing component in this blend, photogeneration is expected to occur predominantly in the TQ₁-rich regions, which can further increase their contribution to the measured photocurrent. As an example, the local I-V curve recorded within the TQ₁-rich matrix is shown in Figure 18.c. Under illumination, the nanoscale junction operates in the second quadrant,

characterized by a negative nanoscale open circuit voltage (nV_{oc}) and a positive nanoscale short-circuit current (nI_{sc}), confirming photovoltaic behavior at the local scale.

Although pc-AFM provides insight into local photocurrent generation, it does not directly provide information on local composition, as is also the case for PF-QNM and KPFM. To obtain chemical information, atomic force microscopy – infrared spectroscopy is briefly introduced in the next section.

4.1.4 Atomic force microscopy – infrared spectroscopy

Atomic Force Microscopy – Infrared spectroscopy (AFM-IR) combines AFM operated in either contact or tapping mode, with a tunable pulsed infrared laser, typically a quantum cascade laser (QCL) as a light source. This combination enables simultaneous acquisition of topographical and chemical information, allowing spatially resolved compositional mapping. AFM-IR measurements can be used either to record local infrared spectra, by measuring the AFM-IR signal as a function of wavenumber, or to generate chemical maps by recording the signal as a function of position at a selected wavenumber [104].

The measurement principle described here refers specifically to the AFM-IR mode used in this work. The IR laser irradiates the sample at the same location as the AFM tip. When the sample absorbs the incident IR radiation, the local temperature increases, which induces a rapid thermal expansion of the material in the absorbing region. This thermal expansion acts as a force impulse on the cantilever and drives it into oscillation. The process relies on the fact that the molecular vibrations excited by absorbed IR photons relax to their ground vibrational state through the transfer of energy to the lattice in the form of heat [105]. The cantilever oscillations are detected by the beam-deflection method in the same manner as in conventional AFM topography measurements, as described in section 4.1. In this work, AFM-IR in tapping mode was used. In this mode, the cantilever is driven at its free resonance frequency (first harmonic), and the laser pulse repetition rate is adjusted to match the difference between this frequency and the first overtone of the cantilever. The topographical signal is derived

from the first harmonic response, while the local chemical IR signal is obtained by deconvolution of the second harmonic response.

Figure 19 shows the AFM height image (a) and the corresponding AFM-IR mappings recorded at 1430 cm^{-1} and 1598 cm^{-1} (b,c), and representative AFM-IR spectra recorded at two distinct regions of the $\text{TQ}_1:\text{PC}_{70}\text{BM}$ (1:3). Based on previous works from our group, the peak at 1430 cm^{-1} corresponds to the vibration of C_{70} cage of PC_{70}BM , whereas 1598 cm^{-1} correspond to aromatic $\text{C}=\text{C}$ stretching mode of the phenyl ring [106, 107]. Consistent with these assignments, the AFM-IR map recorded at 1430 cm^{-1} shows enhanced signal in the globular domains, indicating that these regions are rich in PC_{70}BM , while the map recorded at 1598 cm^{-1} highlights the surrounding matrix, which is therefore assigned as TQ_1 -rich. The spectra acquired in the two regions further support this interpretation through the relative differences in the intensities of these characteristic peaks.

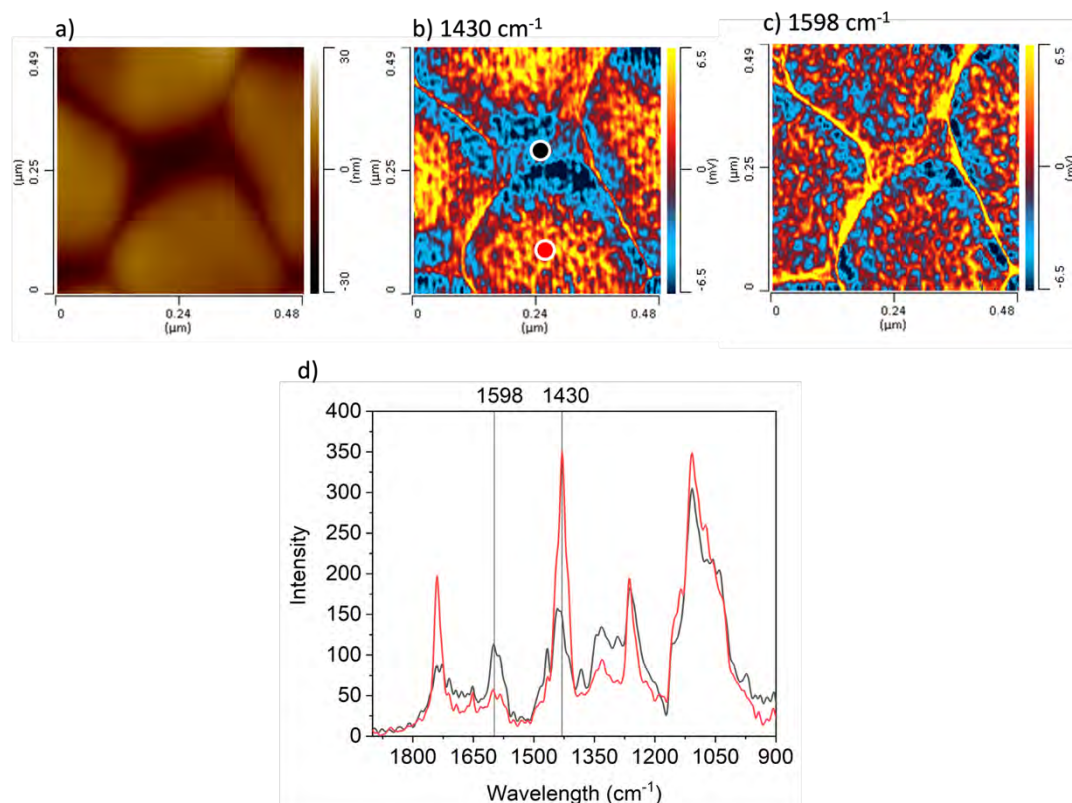


Figure 19. AFM-IR images ($0.48\text{ }\mu\text{m} \times 0.48\text{ }\mu\text{m}$) of $\text{TQ}_1:\text{PC}_{70}\text{BM}$ (1:3) blends prepared from solution in CB. a) Tapping mode height image. b) tapping mode AFM-IR mapping at 1430 cm^{-1} , showing PC_{70}BM -rich regions and c) at 1598 cm^{-1} , showing the TQ_1 rich regions. Measurements and sample processing performed by the author.

Overall, AFM-IR complements the other SPM techniques described in this chapter by adding chemically specific information with nanoscale spatial resolution. While techniques such as PF-QNM, KPFM, and pc-AFM measure local and electrical properties, AFM-IR makes it possible to assign these features to the local chemical composition of the sample. Together, these methods provide a more complete picture of the morphology-property relations in organic semiconductor thin films.

4.2 Near-edge X-ray absorption fine structure spectroscopy

Near-edge X-ray absorption fine structure (NEXAFS) is a spectroscopy technique that examines the absorption of X-rays near the absorption edge of a specific element. It provides detailed information about the electronic structure, chemical bonding, and molecular orientation of materials by analysing transitions of core-electron to unoccupied energy states. By varying the photon energy for the X-ray excitation, different absorption edges can be probed, providing element-specific information. The fine structure in the NEXAFS spectra, specifically the position (i.e. photon energy) of the absorption resonances, reveals the chemical composition of the material.

Absorption resonances occur when a photon has an energy equal to the energy difference between two states involved in an allowed electronic transition. As depicted in Figure 20, the absorption of X-ray photons leads to the excitation of core-level electrons to an unoccupied (molecular) state, creating core holes. To detect this absorption resonance, we probe the relaxation process, when an outer shell electron relaxes to the core level to fill the core hole. The excess of energy from this de-excitation can result in two different events: the emission of a photon (radiative de-excitation, Figure 20.b) or the emission of an Auger electron (non-radiative de-excitation, Figure 20.c)

Due to the directional character of the molecular orbitals, linearly polarized X-rays can be used to determine the molecular orientation of molecules in the sample. This is possible because the resonant absorption intensity for a transition from an atomic ground state to a specific molecular orbital final state depends on the orientation of the electric field vector (\vec{E}) of the electromagnetic radiation with respect to the

transition dipole moment (TDM) of the corresponding electronic transition. The absorption is largest when \vec{E} is aligned with the TDM and vanishes when \vec{E} is perpendicular to it.

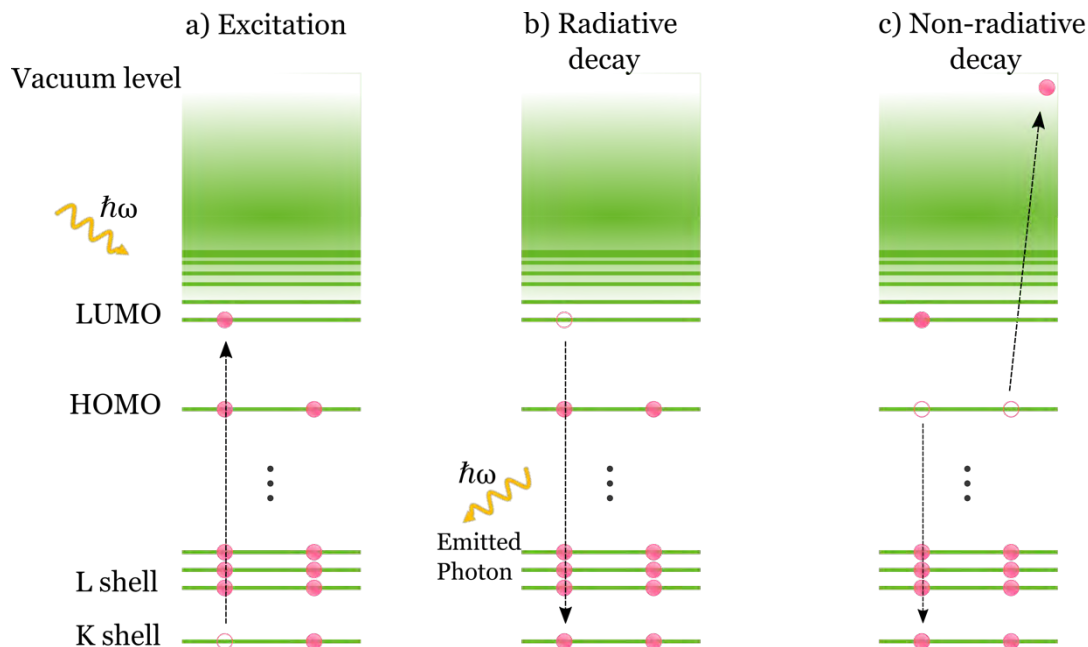


Figure 20. Schematic representation of the photon-absorption and decay channels in NEXAFS. a) A core electron is excited to an unoccupied molecular orbital upon the absorption of an X-ray photon. b) Radiative decay occurs via fluorescence, emission of an X-photon. c) Example of one of the non-radiative decay channels, via emission of an electron, also called spectator decay.

The absorbed X-ray intensity in NEXAFS can be recorded by different detection modes depending on the decay channel. When monitoring the emitted photoelectrons, there are three electron yield detection modes: Auger electron yield (AEY), partial electron yield (PEY), and total electron yield (TEY). In AEY only the electrons with kinetic energy within a narrow range, centred around the Auger peak energy of the investigated edge are considered [108]. The photoelectrons are collected by an electron detector; therefore, this detection mode provides a direct measure of the X-ray absorption cross-section [109]. The fraction of Auger electrons that suffer energy loss due to inelastic scattering have lower kinetic energy than the Auger electrons elastically scattered and are not detected in this mode. PEY is measured by an electron multiplier in combination with retarding grid, which applies a voltage to

selectively block low-energy electrons. In PEY, the kinetic energy range of the detector is larger than for AEY, allowing for the detection of both elastic and inelastic Auger electrons. In TEY, electrons of all energies from the sample are collected, resulting in a signal that is dominated by low kinetic energy electrons. Additionally, for TEY there is an indirect way to record the NEXAFS signal by measuring the sample drain current, using an electrometer. Emitted fluorescent photons are monitored in fluorescence yield (FY), typically using detectors with energy-discriminating ability, such as high-purity Ge or Si solid-state detectors (SSD) and silicon drift diode detectors (SDD).

From the quantum mechanical description of the excitation process within the dipole approximation, the transition probability is proportional to the square of the matrix element between the initial core state and the final unoccupied state. For a $1s$ initial state and a directional final state orbital, the absorption intensity can be written as:

$$I \propto |\mathbf{E} \cdot \mathbf{O}|^2, \quad (12)$$

where \mathbf{E} is the electric field vector of the incident X-ray and \mathbf{O} is the TDM vector associated with the final-state orbital O . For vector-like orbitals such as π^* this reduces to:

$$I \propto \cos^2\delta, \quad (13)$$

where δ is the angle between the electric field vector and the direction of the transition dipole moment. This angular dependence is illustrated schematically in Figure 21 for a diatomic molecule with a directional π -type orbital adsorbed on a surface. Depending on the incidence angle, the projection of the electric field vector onto the π^* or σ^* TDM changes, resulting in different absorption intensities.

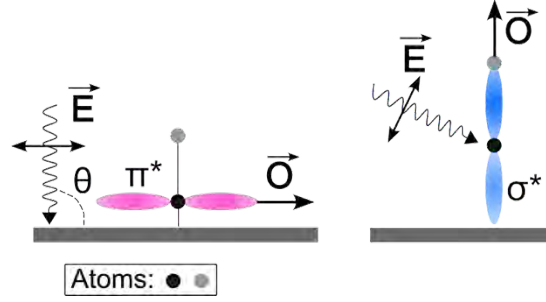


Figure 21. Schematic illustration of the angular dependence of NEXAFS resonances for a π -bound diatomic molecule oriented with its molecular axis perpendicular to the surface. Figure adapted from reference [110]. The absorption intensity is proportional to $|\mathbf{E} \cdot \mathbf{O}|^2$, where \mathbf{O} denotes the transition dipole moment of the final-state orbital. Depending on the incidence angle, the overlap between \mathbf{E} and π^* or σ^* transition dipole moment changes. In this configuration, π^* resonance is maximized at normal incidence (left), while the σ^* resonance is maximized at grazing incidence (left).

The measured intensity, therefore, depends on both the X-ray incidence angle θ with respect to the surface and the average tilt angle α of the molecular π system with respect to the substrate. Following Stöhr and Outka [111], the intensity of X-ray absorption is given by:

$$I = C[P \cdot I^{\parallel} + (1 - P) \cdot I^{\perp}], \quad (14)$$

with

$$I^{\parallel} = A \left(\frac{1}{2} \sin^2 \theta + \cos^2 \alpha \left[\cos^2 \theta - \frac{1}{2} \sin^2 \theta \right] \right), \quad (15)$$

and

$$I^{\perp} = \frac{1}{2} A \sin^2 \alpha, \quad (16)$$

where A is a cross-sectional constant and P is the degree of linear polarization of the incident radiation. By fitting the angular dependence of the π^* resonance intensity using this formula, the average orientation angle α can be determined.

The first term in Equation 15, is independent of molecular tilt angle. All dependence of the absorption intensity molecular orientation is contained in the coefficient of $\cos^2 \alpha$. The absorption intensity becomes independent of the molecular tilt angle α when this coefficient, which depends on the X-ray incidence angle, vanishes. This condition is obtained by solving:

$$\cos^2 \theta - \frac{1}{2} \sin^2 \theta = 0 \quad (17)$$

yields $\cos^2 \theta = \frac{1}{3}$, corresponding to an incidence angle of $\theta=54.7^\circ$ with respect to the surface. This angle is called the magic angle. At the magic angle, the angular dependence of the absorption intensity vanishes, resulting in an orientation-independent signal.

Instead of explicitly determining the molecular tilt angle α , the angular dependence of the intensities of the absorption resonances can be quantified by the dichroic ratio, given by:

$$D = \frac{I_{\perp} - I_{\parallel}}{I_{\perp} + I_{\parallel}}, \quad (18)$$

where I_{\perp} and I_{\parallel} represent the normalized absorption intensity at normal and grazing incidence, respectively. Even if the intensity at grazing incidence can be hard to access experimentally, it can be obtained from the angular dependence of the peak intensity. This is typically done by extrapolating the measured intensities at a series of accessible angles as a function of $\sin^2 \theta$ or $\cos^2 \theta$. For perfectly linearly polarized radiation ($P=1$), the dichroic ratio ranges from -1 to 1, where 1 indicates perfect edge-on orientation, and -1 indicates perfect face-on orientation. A dichroic ratio $D = 0$ indicates either a random molecular orientation or an average tilt angle of 54.7° .

The carbon K-edge NEXAFS spectra of ethene (C_2H_4) are used here as an example to show how this technique provides information on electronic structure, chemical environment, and molecular orientation. Figure 22.a and 22.b show the unoccupied molecular orbitals π^* and σ^* of ethene in the gas phase, respectively. The π^* orbital is oriented perpendicular and the σ^* orbital is parallel to the molecular plane. Additionally, Figure 22 displays the NEXAFS spectra of ethene in the gas phase alongside the measured spectra of ethene on Pt (111) recorded in normal and grazing X-ray incidence. In the carbon K-edge spectrum of ethene in the gas phase (recorded by A. P. Hitchcock), one can see the π^* (~ 285 eV) resonance, a C-H (~ 288 eV) resonance, and a broad σ^*

(~ 300 eV) resonance. The π^* and σ^* resonances are associated with the C-C core of the molecule [109].

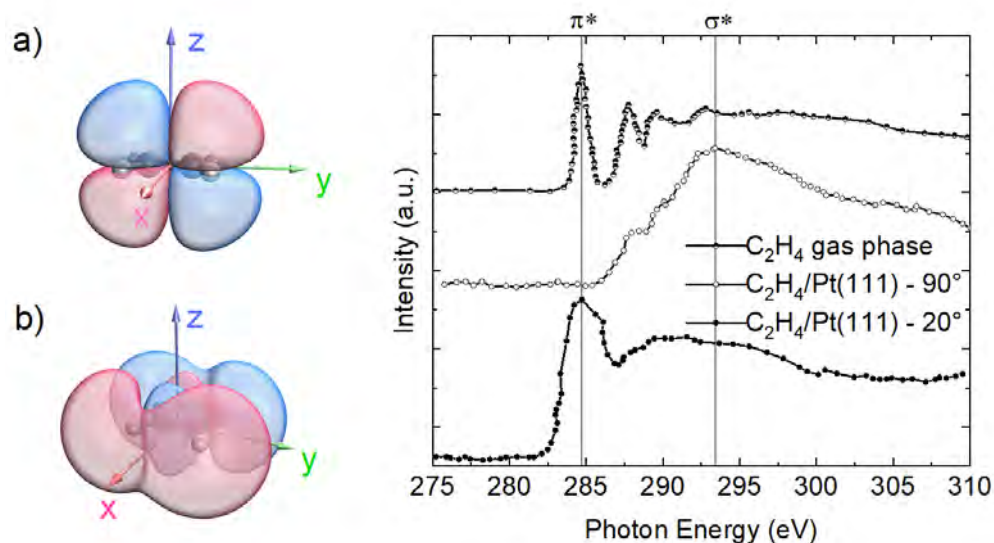


Figure 22. a) π^* and b) σ^* molecular orbitals of ethene (C_2H_4), calculated with B3LYP/6-31G(d,p) theory level in gas phase. (right) NEXAFS spectra of ethylene in gas phase and, ethylene on Pt (111) for grazing and normal X-ray incidence; the spectra were reproduced from reference [109, 112].

When comparing the ethene gas phase spectra to the variable angle spectra of ethylene/Pt(111) [113] one can obtain interesting insights about the chemical environment and molecular orientation of the molecule. The linearly polarized X-ray beam, incident normal to the sample surface (incidence angle 90°) has its oscillating electric field vector aligned parallel to the substrate plane (Figure 21). The vanishing of the π^* resonance and strong σ^* resonance, observed for the NEXAFS spectrum recorded in normal incidence w.r.t to the surface, indicates that ethene has the C-C axis parallel to the substrate. Additionally, for the NEXAFS spectrum recorded in grazing incidence w.r.t the surface, the opposite is observed, the π^* resonance appears much stronger than σ^* resonance, confirming the face-on orientation. One can also observe changes in the resonance features due to the interaction between the ethene molecules and the Pt (111). For instance, the broadening of the π^* resonance peak and C-H resonance peak.

4.3 Time-of-flight secondary ion mass spectrometry (ToF-SIMS)

Secondary ion mass spectrometry (SIMS) is a powerful surface analysis technique that provides information about the sample's chemical composition. Since the first developments in the 1960s by Benninghoven [114], SIMS has found diverse interesting applications in various research fields. For instance, it has been used for cosmochemistry, specifically in the analysis of extraterrestrial samples [115, 116].

In SIMS, the sample surface is bombarded by a primary beam of high-energy ions (between 1 keV and 25 keV) that lead to the sputtering of neutral and charged atoms or clusters of atoms from the sample surface, the so-called secondary ion beam. The primary ions are usually Bi^+ , Ar^+ , Ga^+ , or Cs^+ . The interaction of the primary ions with the sample surface results in the emission of secondary particles, of which only 1% is ionized and become the secondary ions that are analyzed in SIMS [117]. There are two operational modes of SIMS: static and dynamic SIMS. Static SIMS uses a low flux of primary ions ($<2.7 \text{ nA cm}^{-2}$). It is used for surface analysis composition, keeping the damage of the surface area as low as possible. In dynamic SIMS, a high flux of primary ion ($>1 \text{ }\mu\text{A cm}^{-2}$) is used. This high flux promotes the erosion of the surface, removing layer by layer. The secondary ions are continuously analyzed to provide an elemental distribution in a depth profile.

The secondary ions need to be collected and analyzed by a mass analysis system, which separates secondary ions according to their ratios of mass to electric charge $\left(\frac{m}{z}\right)$ [118]. There are different types of mass analyzers, such as magnetic sector analyzer, quadrupole analyzer, and time-of-flight (ToF) analyzer. In this work, the mass analysis system used was ToF. ToF is based on the fact that ions of different masses and same kinetic energy have different times of flight to the detector. In the ToF spectrometer, ions of charge q , typically ± 1 , are subjected to an extraction field, V_e , setting each ion with a fixed kinetic energy, E_k . Considering $E_k = \frac{mv^2}{2}$, as E_k is constant for all ions, the velocity of each ion is inversely proportional to its mass (m) [119]. Therefore, the heavier the ion, the slower its travel towards the detector. Considering a flight

tube of path length l , the flight time of an ion through the flight tube can be determined by:

$$t = l(2V_e)^{-1/2} \left(\frac{m}{z}\right)^{1/2} \quad (19)$$

ToF-SIMS can be applied to obtain information on the sample chemistry as function of depth, i.e. dynamic SIMS. In this case, separate ion beams are used for etching and analysis purposes [117]. The primary beam continuously analyzes the bottom of the crater generated by the sputter ion beam (O_2 , Cs ions or clusters of Ar_n or O_{2n}). The data is acquired as a function of sputtering time, and one can convert this into depth by using the relation:

$$Y = \frac{dD}{dF} \quad (20)$$

Here, Y is the sputtering yield, indicating the number of target atoms removed per incident sputtering ion [118]. D represents the crater depth and F the sputtering ion dose. Additionally, the secondary ion intensity of elements is plotted against the depth or sputtering time.

One of the main advantages of SIMS over electron spectroscopies is its ability to detect all chemical elements in the periodic table, including hydrogen, as well as isotopes and molecular species. This, combined with the detection of elements in concentrations as low as 10^{-6} , makes SIMS a unique characterization technique [117]. For multicomponent donor-acceptor systems, nanometer-scale depth profiling is especially useful for characterizing vertical stratification. However, SIMS depth profiles should not be interpreted as a direct measure of the true composition profile, since they can be affected by several artifacts. Ion-beam-induced mixing and recoil implantation (“knock-in” effects) can broaden interfaces, while different sputter rates of the individual components may distort apparent layer thicknesses and interface positions [120]. Moreover, matrix effects cause the secondary-ion intensities to depend on the local chemical environment, meaning that the choice of positive or negative secondary ions can influence sensitivity and that the detected signal is not always directly proportional to concentration [121]. Additional artifacts may arise near organic/ inorganic interfaces or silicon substrates [120].

5 Summary of the Publications

5.1 Paper 1

The role of the solvent on the orientation of Y-type acceptor molecules in spin-coated films

Leticia P. Christopholi, Cleber F. N. Marchiori, Ishita Jalan, Andreas Opitz, Stela Andrea Muntean, Ellen Moons

The Journal of Physical Chemistry C 128.42 (2024): 17825-17835.

In this paper, the influence of the processing solvent on the molecular orientation of the acceptor molecules Y5 and Y6 in unannealed acceptor-only spin-coated films was investigated. We applied the Hansen solubility parameters (HSP) model as a tool to make a rational solvent selection for Y5 and Y6. Based on the calculated HSP values, three solvents were selected for the study: chlorobenzene (CB), chloroform (CF), and ortho-xylene (o-XYL). The orientation of the conjugated π -system of the molecules in the spin-coated films was investigated by NEXAFS spectroscopy. The total electron yield mode (TEY) was used to probe the molecular orientation at the surface, and the fluorescence yield mode (FY) was used to obtain information from deeper into the bulk of the film. It was found that not all the solvents commonly used to process those materials led to preferential face-on orientation, which is the desired orientation for both improved light absorption and vertical charge transport in organic solar cells. TD-DFT calculations at the carbon and nitrogen K-edges were used to assign the electronic transitions observed in the NEXAFS spectra. The angular dependence of the NEXAFS resonances showed that Y5 and Y6 exhibit a preferential face-on orientation when processed from the CF solution, whereas films prepared from CB and o-XYL solutions do not show this preference. This effect results from the competition between solute-solvent and solute-solute interactions, which influence the film formation and ultimately determine the final morphology. CF, as the better solvent, promotes stronger solvent-solute interactions and favors face-on orientation, while CB and o-XYL promote stronger solute-solute interactions and pre-aggregation in solution, which hinders molecular ordering in the final film.

5.2 Paper 2

Probing molecular orientation of donors and acceptors in all polymer blends.

Leticia P. Christopholi, Zewdneh Genene, Cleber F. N. Marchiori, Stela Andrea Muntean, Ergang Wang, Ellen Moons

Journal of Physics: Materials. 9 (2026) 025001

Understanding the microstructure of electron-donor and electron-acceptor materials is crucial for optimizing the performance of all-polymer solar cells. In this study, near-edge X-ray absorption fine structure (NEXAFS) spectroscopy was employed to investigate the molecular orientation of spin-coated thin films of the polymers PF5-Y5 and PYT, as well as their blends with PBDB-T in donor: acceptor ratios of 1:0.75 and 1:10. The comparison of NEXAFS spectra acquired in partial electron yield (PEY), total electron yield (TEY), and fluorescence yield (FY) modes provides depth-dependent information about the films. The carbon K-edge spectra in PEY mode of all the blend films resembled the spectral signatures of the donor PBDB-T, indicating that the blend film surface is PBDB-T-rich, even at a tenfold higher acceptor concentration. To identify the acceptor component in the carbon spectra, deeper subsurface probing was required using the TEY and FY modes, along with analysis of the angular dependence of these spectra. Nitrogen K-edge NEXAFS spectra were employed to selectively probe the acceptor orientation in the blend films, revealing that PBDB-T: PF5-Y5 (1:0.75), PBDB-T: PF5-Y5 (1:10), and PBDB-T: PYT (1:10) blends retain the face-on orientation observed in neat acceptor films. However, for the PBDB-T: PYT (1:0.75) blend, a reduced dichroic ratio for the first nitrogen $1s \rightarrow \pi^*$ resonance at 398.56 eV in PEY spectra indicates that the donor PBDB-T influences the molecular orientation of PYT in the film's surface layer. Notably, this work demonstrates a novel approach, using the dichroism at selective absorption edges, to access the molecular orientation of one of the components in a polymer blend film.

5.3 Paper 3

Sequential Deposition Enables Suppression of Spontaneous Donor Enrichment of the Surface in Spin-coated Films

Leticia P. Christopholi, Paweł Dąbczyński, Saurabh Pareek, Ewa Partyka – Jankowska, Marcin Zając, Stela Andrea Muntean, Ellen Moons
Journal of Physics: Materials. 9 (2026) 015018

In this work, time-of-flight secondary ion mass spectrometry (ToF-SIMS) was employed to investigate the vertical distribution of sequentially deposited PM6/Y5 films and of blend PM6:Y5 films coated in a one-step process. The influence of thermal annealing (TA) on the vertical distribution of the components was also evaluated. The depth-profiles revealed that blend-casting samples present a donor-rich surface layer, approximately 2.4 nm wide, and that TA does not affect this vertical composition. On the other hand, the depth profiles of the sequentially deposited films show that sequential deposition (SD) promotes an acceptor-rich surface layer. It was found that thermal annealing of the PM6 bottom layer before further processing helps to suppress Y5 diffusion into this layer, and TA after the acceptor layer was deposited further promotes vertical phase separation, resulting in a composition gradient with Y5 enrichment near the surface and PM6 content closer to the bottom. Additionally, near edge X-ray absorption fine structure (NEXAFS) spectroscopy was used to investigate the composition and the molecular orientation of the donor PM6 and the acceptor Y5 in blend and SD films. Depth-dependent molecular orientation was assessed by comparing NEXAFS spectra acquired in total electron yield (TEY) and fluorescence yield (FY). For PM6:Y5 blends measured in TEY mode the carbon K-edge spectrum was dominated by spectral features of the donor PM6, while for SD-films, they are dominated by Y5 spectral features, clearly reflecting the donor-rich and acceptor-rich surfaces, in agreement with ToF-SIMS results. Furthermore, nitrogen K-edge NEXAFS spectra were employed to selectively probe the acceptor orientation. In SD-processed samples, NEXAFS nitrogen K-edge spectra recorded in TEY and FY modes showed that Y5 retains its face-on orientation when deposited on top of PM6, despite the combined effects of film formation dynamics and interfacial intermixing inherent to the process. A similar behavior was observed for PM6:Y6 blends, although the dichroic response at the surface was reduced.

5.4 Paper 4

Unravelling Sulphur L₁-Edge NEXAFS Spectra of Thiophene-based Organic Semiconductors

Leticia P. Christopholi, Robert Temperton, Alexei Preobrajenski, Stela Andrea Muntean, Ellen Moons, Cleber F. N. Marchiori

Manuscript

In this work, the sulfur L₁ absorption edge was investigated as an alternative soft X-ray probe for studying molecular orientation in sulfur-containing conjugated polymers. The motivation was to evaluate whether the L₁-edge can be used as a more accessible and simpler spectroscopic probe compared to the sulfur K-edge at hard X-ray photon energies and the more complex L_{2,3}-edges.

Angle-dependent NEXAFS measurements were performed on neat films of two acceptor-type polymers, PYT and PF5-Y5, and the interpretation of the spectra was supported by time-dependent density functional theory (TD-DFT) calculations. Although sulfur atoms in different chemical environments exhibit nearly identical spectral features in L₁-edge spectra, distinct differences in angular response were observed. PYT exhibited clear dichroism, consistent with previously reported face-on orientation trends from carbon K-edge and nitrogen K-edge measurements, whereas PF5-Y5 showed reduced dichroism due to its more complex electronic structure.

The theoretical analysis revealed that the interpretation of sulfur L₁-edge spectra is not straightforward. The intense low-energy resonance consists of multiple transitions with mixed character, including significant $\sigma^*(\text{S-C})$ contributions as well as π^* -type states associated with the conjugated backbone. This mixed nature closely parallels previous interpretations reported for the sulfur K-edge of organic materials and demonstrates that the dominant peak cannot be assigned to a purely π^* or σ^* transition.

Overall, this study establishes practical guidelines for interpreting sulfur L₁-edge spectra and shows that its reliability for probing molecular orientation depends on the electronic structure of the specific polymer. The results highlight both the potential and the limitations of using the sulfur L₁-edge for molecular orientation analysis in conjugated materials.

5.5 Paper 5

Nanoscale Study of Surface Photovoltage, Photocurrent, and Nanomechanical Properties on Finely Mixed Blend Films.

Leticia P. Christopholi, Ismail Benamar, Stela Andrea Muntean, Philippe Leclere and Ellen Moons

Manuscript

In this work, AFM-based techniques were applied to the benchmark non-fullerene PBDB-T:Y6 system to investigate nanoscale electrical and mechanical properties under different processing conditions. Kelvin probe force microscopy (KPFM), photoconductive AFM (pc-AFM) were used to probe surface potential and local photocurrent generation, while PeakForce quantitative nanomechanical mapping (PF-QNM) provided nanomechanical contrast. The results show that the intermixed morphology characteristic of modern donor:NFA blend systems makes it difficult to directly assign the observed electrical or mechanical contrast to composition, and hence to distinct donor- or acceptor-rich domains. This work discusses the challenges faced when employing AFM-based techniques for investigating nanoscale structure-property relationships in high-performance organic photovoltaic blends.

6 Conclusions

Morphology in organic photovoltaic active layers has long been recognized as a key factor governing device performance. With the development of new and planar electron-donor and electron-acceptor materials, additional research questions arise regarding not only nanoscale morphology, but also molecular orientation. At the same time, the current availability of a range of advanced characterization techniques has opened new possibilities for understanding how processing conditions influence molecular orientation and nanoscale structure.

One of the main findings of this thesis is that solvent choice can influence molecular orientation, but that its effect cannot be generalized across different materials systems. For the small molecule acceptors Y5 and Y6, chloroform (CF) yields smooth films with pronounced face-on orientation, whereas chlorobenzene (CB) and ortho-xylene resulted in non-oriented films. This behavior contrasts with reports for organic semiconductor systems, in which higher boiling point solvents are often associated with enhanced molecular orientation due to a slower drying rate. Our findings show that when solute-solute interactions dominate over solvent-solute interactions, pre-aggregation occurs already in solution, which can hinder the molecular orientation during film formation. In contrast, polymer derivatives based on Y5, such as PYT and PF5-Y5, exhibited face-on orientation when processed from CB. Overall, these results show that processing guidelines for small molecules cannot be directly transferred to their polymer derivatives. Instead, the effect of solvent must be evaluated for each material individually, since it depends on its intermolecular interactions and the aggregation behavior of the system.

By combining the nitrogen K-edge with depth-dependent detection modes, it was possible to selectively probe the orientation of the acceptors PYT and PF5-Y5 in blend films. The results showed that the acceptors retained their face-on molecular orientation even after blending with the donor PBDB-T, which did not exhibit preferential orientation. This information is not accessible from the carbon K-edge, where both components contribute to the spectra. This approach was also applied to PM6/Y5 films processed by sequential deposition rather than

conventional one-step blend-casting, confirming that the acceptor retained its face-on orientation despite the interfacial intermixing during film formation. Together, these results show that element-specific absorption edges are essential for resolving the orientation of individual components in multicomponent donor-acceptor systems.

In addition, this work evaluates the sulphur L₁-edge as a more accessible alternative soft X-ray to the sulphur K-edge and as a simpler spectroscopic probe than the sulfur L_{2,3} edges for studying organic semiconductors. For PYT, the spectra showed a dichroic response consistent with carbon K-edge measurements, whereas PF5-Y5 exhibited low dichroic response due to its more complex structure. Supported by TD-DFT calculations, the analysis revealed both the potential and the limitations of this edge. In particular, the intense low-energy resonance comprises multiple transitions of mixed character, including significant $\sigma^*(\text{S}-\text{C})$ contributions and π^* -type states associated with the conjugated backbone, which makes peak assignment nontrivial. A broader conclusion is therefore that the sulphur L₁-edge is a promising probe for molecular orientation, especially for sulfur-containing systems with simpler electronic structure, such as small molecules, where the spectral features may be easier to interpret.

Another important outcome of this thesis is that vertical stratification can be intentionally modified through deposition methods and post-processing treatments. Sequential deposition was investigated as a strategy to control vertical phase separation in PM6-Y5 systems, which, when processed via blend casting, exhibit a donor-rich surface. Sequential deposition inverts vertical distribution within the active layer, while thermal annealing helps to suppress Y5 diffusion into the PM6 layer, resulting in acceptor-rich surfaces. Such control over vertical stratification is particularly relevant for conventional device architectures, where acceptor-rich surfaces facilitate electron extraction.

Macroscopic device measurements and structural characterization provide valuable information on structure-performance relations in organic solar cells, but they do not directly reveal photovoltaic behavior at the nanoscale. To address this, complementary AFM-based techniques were applied to PBDB-T:Y6 blends. PF-QNM, KPFM, and pc-

AFM, to probe nanomechanical, surface potential, and photocurrent generation, respectively. The finely intermixed structure of these modern non-fullerene systems implies that domain sizes are often approaching or falling below the spatial resolution of the techniques. This limits the direct assignment of nanomechanical and electrical signals to composition, and hence correlation with distinct donor-or acceptor-rich domains. The findings highlight the importance of combining complementary characterization techniques and careful data interpretation.

Overall, this work demonstrates that a comprehensive understanding of morphology in organic solar cells requires the combination of element-selective spectroscopy and nanoscale probe techniques, while critically assessing their strengths and limitations. The findings contribute to a more robust experimental framework for the investigation of molecular orientation and nanoscale structures in organic photovoltaic materials.

7 References

1. (2025), I. *World Energy Outlook 2025*, IEA, Paris. 2025.
2. Agency, I.E. *Net Zero Roadmap: A Global Pathway to Keep the 1.5° C Goal in Reach*. 2023. IEA Paris, France.
3. Administration), N.N.O.a.A., *Energy on a Sphere - NOAA*. 2015.
4. IRENA, *Renewable capacity statistics 2025*, International Renewable Energy Agency, Abu Dhabi. 2025.
5. Masson, G., et al., *Snapshot of global PV markets 2025*. (No Title), 2025: p. p 24.
6. Zaidi, B., *Introductory chapter: Introduction to photovoltaic effect*. Solar Panels and Photovoltaic Materials, 2018: p. 1-8.
7. Gaëtan Masson, M.d.l.E., Izumi Kaizuka, Junko Okazaki, *Trends in PV Applications 2025*. 2025.
8. Shi, Y., J.J. Berry, and F. Zhang, *Perovskite/silicon tandem solar cells: insights and outlooks*. ACS Energy Letters, 2024. **9**(3): p. 1305-1330.
9. Li, Y., et al., *Recent progress in organic solar cells: a review on materials from acceptor to donor*. Molecules, 2022. **27**(6): p. 1800.
10. Kallmann, H. and M. Pope, *Photovoltaic effect in organic crystals*. The Journal of Chemical Physics, 1959. **30**(2): p. 585-586.
11. Tang, C.W., *Two-layer organic photovoltaic cell*. Applied physics letters, 1986. **48**(2): p. 183-185.
12. Sariciftci, N.S., *Role of buckminsterfullerene, C60, in organic photoelectric devices*. Progress in Quantum Electronics, 1995. **19**(2): p. 131-159.
13. Halls, J., et al., *Efficient photodiodes from interpenetrating polymer networks*. Nature, 1995. **376**(6540): p. 498-500.
14. Heeger, A.J., *25th anniversary article: bulk heterojunction solar cells: understanding the mechanism of operation*. Advanced materials, 2014. **26**(1): p. 10-28.
15. Liu, J., et al., *Solution Sequential Deposition Pseudo-Planar Heterojunction: An Efficient Strategy for State-of-Art Organic Solar Cells*. Small Methods, 2024: p. 2301803.
16. *Single-junction organic solar cells with a power conversion efficiency of more than 20%*. Nature Energy, 2024. **9**(8): p. 930-931.
17. Jiang, Y., et al., *20.6% efficiency organic solar cells enabled by incorporating a lower bandgap guest nonfullerene acceptor without open-circuit voltage loss*. Advanced Materials, 2025. **37**(17): p. 2500282.
18. Dong, J., et al., *Dielectric constant engineering of nonfullerene acceptors enables a record fill factor of 83.58% and a high efficiency of 20.80% in organic solar cells*. Energy & Environmental Science, 2025. **18**(10): p. 4982-4995.
19. Li, C., et al., *Non-fullerene acceptors with high crystallinity and photoluminescence quantum yield enable > 20% efficiency organic solar cells*. Nature Materials, 2025. **24**(3): p. 433-443.
20. Duan, X., et al., *Over 20.5% Efficiency of Halogen-Free Solvent-Processed Organic Solar Cells Achieved by Anti-Solvent Strategy*. Advanced Materials, 2026. **38**(4): p. e14076.

21. Guan, S., et al., *Self-assembled interlayer enables high-performance organic photovoltaics with power conversion efficiency exceeding 20%*. *Advanced Materials*, 2024. **36**(25): p. 2400342.
22. Bi, P., et al., *Progress in organic solar cells: materials, physics and device engineering*. *Chinese Journal of Chemistry*, 2021. **39**(9): p. 2607-2625.
23. Ala'a, F.E., et al., *Recent advances of non-fullerene, small molecular acceptors for solution processed bulk heterojunction solar cells*. *Journal of Materials Chemistry A*, 2014. **2**(5): p. 1201-1213.
24. Atkins, P.W., J. De Paula, and J. Keeler, *Atkins' physical chemistry*. 2023: Oxford university press.
25. Shirakawa, H., T. Masuda, and K. Takeda, *Synthesis and properties of acetylenic polymers*. *Triple Bonded Functional Groups* (1994), 1994: p. 945-1016.
26. Brabec, C.J., et al., *Organic photovoltaics: concepts and realization*. Vol. 60. 2003: Springer Science & Business Media.
27. Liu, Y., et al., *Probing the nature of charge carriers in one-dimensional conjugated polymers: a review of the theoretical models, experimental trends, and thermoelectric applications*. *Journal of Materials Chemistry C*, 2023. **11**(1): p. 12-47.
28. Salaneck, W.R., R.H. Friend, and J.L. Brédas, *Electronic structure of conjugated polymers: consequences of electron–lattice coupling*. *Physics reports*, 1999. **319**(6): p. 231-251.
29. Sze, S.M., Y. Li, and K.K. Ng, *Physics of semiconductor devices*. 2021: John wiley & sons.
30. Köhler, A. and H. Bässler, *Electronic processes in organic semiconductors: An introduction*. 2015: John Wiley & Sons.
31. Hains, A.W., et al., *Molecular semiconductors in organic photovoltaic cells*. *Chemical reviews*, 2010. **110**(11): p. 6689-6735.
32. Tiwari, S., et al., *Advances in polymer-based photovoltaic cells: Review of pioneering materials, design, and device physics*. *Handbook of Ecomaterials*, 2018. **2**: p. 1055-1101.
33. Dyer-Smith, C., J. Nelson, and Y. Li, *Organic solar cells*, in *McEvoy's Handbook of Photovoltaics*. 2018, Elsevier. p. 567-597.
34. Mikhnenko, O.V., P.W. Blom, and T.-Q. Nguyen, *Exciton diffusion in organic semiconductors*. *Energy & Environmental Science*, 2015. **8**(7): p. 1867-1888.
35. Firdaus, Y., et al., *Long-range exciton diffusion in molecular non-fullerene acceptors*. *Nature communications*, 2020. **11**(1): p. 5220.
36. Hume, P.A., W. Jiao, and J.M. Hodgkiss, *Long-range exciton diffusion in a non-fullerene acceptor: approaching the incoherent limit*. *Journal of Materials Chemistry C*, 2021. **9**(4): p. 1419-1428.
37. Sajjad, M.T., et al., *Long-range exciton diffusion in non-fullerene acceptors and coarse bulk heterojunctions enable highly efficient organic photovoltaics*. *Journal of Materials Chemistry A*, 2020. **8**(31): p. 15687-15694.
38. Riley, D.B., et al., *Efficient Nanoscale Exciton Transport in Non-Fullerene Organic Solar Cells Enables Reduced Bimolecular Recombination of Free Charges*. *Advanced Materials*, 2023. **35**(24): p. 2211174.

39. Zhu, Y., et al., *Exciton binding energy of non-fullerene electron acceptors*. Advanced Energy and Sustainability Research, 2022. **3**(4): p. 2100184.
40. Puschnig, P. and C. Ambrosch-Draxl, *Excitons in organic semiconductors*. Comptes rendus physique, 2009. **10**(6): p. 504-513.
41. Coropceanu, V., et al., *Charge transport in organic semiconductors*. Chemical reviews, 2007. **107**(4): p. 926-952.
42. Yu, G., et al., *Polymer photovoltaic cells: enhanced efficiencies via a network of internal donor-acceptor heterojunctions*. Science, 1995. **270**(5243): p. 1789-1791.
43. Coakley, K.M. and M.D. McGehee, *Conjugated polymer photovoltaic cells*. Chemistry of materials, 2004. **16**(23): p. 4533-4542.
44. McDowell, C., et al., *Solvent additives: key morphology-directing agents for solution-processed organic solar cells*. Advanced Materials, 2018. **30**(33): p. 1707114.
45. Yang, X., *Semiconducting Polymer Composites: Principles, Morphologies, Properties and Applications*. 2012: John Wiley & Sons.
46. Nilsson, S., et al., *Morphology and phase segregation of spin-casted films of polyfluorene/PCBM blends*. Macromolecules, 2007. **40**(23): p. 8291-8301.
47. Liang, R.Z., et al., *Higher mobility and carrier lifetimes in solution-processable small-molecule ternary solar cells with 11% efficiency*. Advanced Energy Materials, 2019. **9**(7): p. 1802836.
48. Zhang, H., et al., *Role of interface properties in organic solar cells: from substrate engineering to bulk-heterojunction interfacial morphology*. Materials Chemistry Frontiers, 2020. **4**(10): p. 2863-2880.
49. Zhao, F., C. Wang, and X. Zhan, *Morphology control in organic solar cells*. Advanced Energy Materials, 2018. **8**(28): p. 1703147.
50. Moons, E., *Conjugated polymer blends: linking film morphology to performance of light emitting diodes and photodiodes*. Journal of Physics: Condensed Matter, 2002. **14**(47): p. 12235.
51. Li, M., et al., *Sequential deposition enables high-performance nonfullerene organic solar cells*. Materials Chemistry Frontiers, 2021. **5**(13): p. 4851-4873.
52. Jing, J., et al., *Solution sequential deposited organic photovoltaics: From morphology control to large-area modules*. eScience, 2023. **3**(4): p. 100142.
53. Song, Y., et al., *Semitransparent organic solar cells enabled by a sequentially deposited bilayer structure*. ACS applied materials & interfaces, 2020. **12**(16): p. 18473-18481.
54. Weng, K., et al., *Optimized active layer morphology toward efficient and polymer batch insensitive organic solar cells*. Nature communications, 2020. **11**(1): p. 2855.
55. Liu, S., et al., *Printable and large-area organic solar cells enabled by a ternary pseudo-planar heterojunction strategy*. Advanced Functional Materials, 2020. **30**(36): p. 2003223.
56. Zhan, L., et al., *Layer-by-layer processed ternary organic photovoltaics with efficiency over 18%*. Advanced Materials, 2021. **33**(12): p. 2007231.
57. Chanda, M., *Introduction to polymer science and chemistry: a problem-solving approach*. 2006: CRC press.

58. Sperling, L.H., *Introduction to physical polymer science*. 2005: John Wiley & Sons.
59. Bates, F.S., *Polymer-polymer phase behavior*. Science, 1991. **251**(4996): p. 898-905.
60. Shaheen, A., et al., *Materials interface engineering: impact of interfacial molecular orientation on organic electronic devices*. Advanced Functional Materials, 2025. **35**(47): p. 2505173.
61. Osaka, I. and K. Takimiya, *Backbone orientation in semiconducting polymers*. Polymer, 2015. **59**: p. A1-A15.
62. Hunter, C.A. and J.K. Sanders, *The nature of π - π interactions*. Journal of the American Chemical Society, 1990. **112**(14): p. 5525-5534.
63. Brinkmann, M., *Structure and morphology control in thin films of regioregular poly(3-hexylthiophene)*. Journal of Polymer Science Part B: Polymer Physics, 2011. **49**(17): p. 1218-1233.
64. Fan, Q., et al., *Over 14% efficiency all-polymer solar cells enabled by a low bandgap polymer acceptor with low energy loss and efficient charge separation*. Energy & Environmental Science, 2020. **13**(12): p. 5017-5027.
65. Xia, X., et al., *Revealing the crystalline packing structure of Y6 in the active layer of organic solar cells: the critical role of solvent additives*. Journal of Materials Chemistry A, 2023. **11**(40): p. 21895-21907.
66. Ma, Y., et al., *Efficient organic solar cells from molecular orientation control of M-series acceptors*. Joule, 2021. **5**(1): p. 197-209.
67. Sirringhaus, H., et al., *Two-dimensional charge transport in self-organized, high-mobility conjugated polymers*. Nature, 1999. **401**(6754): p. 685-688.
68. Lu, C., et al., *Interplay of molecular orientation, film formation, and optoelectronic properties on isoindigo-and thienoisindigo-based copolymers for organic field effect transistor and organic photovoltaic applications*. Chemistry of Materials, 2015. **27**(19): p. 6837-6847.
69. Fu, Y., et al., *Molecular orientation-dependent energetic shifts in solution-processed non-fullerene acceptors and their impact on organic photovoltaic performance*. Nature Communications, 2023. **14**(1).
70. Nahid, M.M., et al., *NEXAFS spectroscopy of conjugated polymers*. European Polymer Journal, 2016. **81**: p. 532-554.
71. Zhou, K., K. Xian, and L. Ye, *Morphology control in high-efficiency all-polymer solar cells*. InfoMat, 2022. **4**(4): p. e12270.
72. P Christopholi, L., et al., *Role of the Solvent on the Orientation of Y-Type Acceptor Molecules in Spin-Coated Films*. The Journal of Physical Chemistry C, 2024. **128**(42): p. 17825-17835.
73. Qian, D., et al., *Design, application, and morphology study of a new photovoltaic polymer with strong aggregation in solution state*. Macromolecules, 2012. **45**(24): p. 9611-9617.
74. He, K., et al., *Wide bandgap polymer donors for high efficiency non-fullerene acceptor based organic solar cells*. Materials Advances, 2021. **2**(1): p. 115-145.
75. Zheng, Z., et al., *PBDB-T and its derivatives: A family of polymer donors enables over 17% efficiency in organic photovoltaics*. Materials Today, 2020. **35**: p. 115-130.

76. Yuan, J., et al., *Single-Junction Organic Solar Cell with over 15% Efficiency Using Fused-Ring Acceptor with Electron-Deficient Core*. *Joule*, 2019. **3**(4): p. 1140-1151.
77. Cui, Y., et al., *Single-junction organic photovoltaic cell with 19% efficiency*. *Advanced Materials*, 2021. **33**(41): p. 2102420.
78. Zhu, L., et al., *Single-junction organic solar cells with over 19% efficiency enabled by a refined double-fibril network morphology*. *Nature Materials*, 2022. **21**(6): p. 656-663.
79. Shoace, S., et al., *What we have learnt from PM6: Y6*. *Advanced Materials*, 2024. **36**(20): p. 2302005.
80. Yuan, J., et al., *Fused Benzothiadiazole: A Building Block for n-Type Organic Acceptor to Achieve High-Performance Organic Solar Cells*. *Advanced Materials*, 2019. **31**(17): p. 1807577.
81. Wei, Q., et al., *A-DA'D-A non-fullerene acceptors for high-performance organic solar cells*. *Science China Chemistry*, 2020. **63**(10): p. 1352-1366.
82. Yuan, J., et al., *Enabling low voltage losses and high photocurrent in fullerene-free organic photovoltaics*. *Nature communications*, 2019. **10**(1): p. 570.
83. Lee, J.-W., et al., *Linker engineering of dimerized small molecule acceptors for highly efficient and stable organic solar cells*. *ACS Energy Letters*, 2023. **8**(3): p. 1344-1353.
84. Wang, W., et al., *Controlling molecular mass of low-band-gap polymer acceptors for high-performance all-polymer solar cells*. *Joule*, 2020. **4**(5): p. 1070-1086.
85. Sahu, N., B. Parija, and S. Panigrahi, *Fundamental understanding and modeling of spin coating process: A review*. *Indian Journal of Physics*, 2009. **83**(4): p. 493-502.
86. Meyerhofer, D., *Characteristics of resist films produced by spinning*. *Journal of Applied Physics*, 1978. **49**(7): p. 3993-3997.
87. Birnie III, D.P., *Rational solvent selection strategies to combat striation formation during spin coating of thin films*. *Journal of Materials Research*, 2001. **16**(4): p. 1145-1154.
88. Binnig, G., C.F. Quate, and C. Gerber, *Atomic force microscope*. *Physical review letters*, 1986. **56**(9): p. 930.
89. Meyer, E., H.J. Hug, and R. Bennewitz, *Scanning probe microscopy*. Vol. 4. 2003: Springer.
90. Voigtländer, B., *Atomic force microscopy*. 2019: Springer.
91. Magonov, S., V. Elings, and M.-H. Whangbo, *Phase imaging and stiffness in tapping-mode atomic force microscopy*. *Surface science*, 1997. **375**(2-3): p. L385-L391.
92. TUNA, C.M.B., *Simultaneous Electrical and Mechanical Property Mapping at the Nanoscale with PeakForce TUNA*.
93. Derjaguin, B.V., V.M. Muller, and Y.P. Toporov, *Effect of contact deformations on the adhesion of particles*. *Journal of Colloid and interface science*, 1975. **53**(2): p. 314-326.
94. Pittenger, B., N. Erina, and C. Su, *Quantitative mechanical property mapping at the nanoscale with PeakForce QNM*. Bruker application note AN128, Rev. A, 2010. **128**: p. 1-12.

95. Hansson, R., et al., *Vertical and lateral morphology effects on solar cell performance for a thiophene–quinoxaline copolymer: PC 70 BM blend*. Journal of Materials Chemistry A, 2015. **3**(13): p. 6970-6979.
96. Hedley, G.J., et al., *Determining the optimum morphology in high-performance polymer-fullerene organic photovoltaic cells*. Nature communications, 2013. **4**(1): p. 2867.
97. Musumeci, C., et al., *Multiparameter investigation of bulk heterojunction organic photovoltaics*. RSC advances, 2017. **7**(73): p. 46313-46320.
98. Benamar, I., *Characterization of Conjugated Polymer Blends for Organic Photovoltaics*, in *Department of Physics*. 2025, University of Mons: Unpublished.
99. Zahmatkeshsaredorahi, A., D.S. Jakob, and X.G. Xu, *Pulsed force kelvin probe force Microscopy— A new type of kelvin probe force microscopy under ambient conditions*. The Journal of Physical Chemistry C, 2024. **128**(24): p. 9813-9827.
100. Sadewasser, S. and T. Glatzel, *Kelvin probe force microscopy*. Vol. 8. 2012: Springer.
101. Grévin, B., et al., *Dual-heterodyne Kelvin probe force microscopy*. Beilstein Journal of Nanotechnology, 2023. **14**(1): p. 1068-1084.
102. Ellison, D.J., et al., *Determination of quasi-fermi levels across illuminated organic donor/acceptor heterojunctions by kelvin probe force microscopy*. Journal of the American Chemical Society, 2011. **133**(35): p. 13802-13805.
103. Grévin, B., et al., *High-resolution noncontact AFM and Kelvin probe force microscopy investigations of self-assembled photovoltaic donor–acceptor dyads*. Beilstein Journal of Nanotechnology, 2016. **7**(1): p. 799-808.
104. Dazzi, A. and C.B. Prater, *AFM-IR: Technology and applications in nanoscale infrared spectroscopy and chemical imaging*. Chemical reviews, 2017. **117**(7): p. 5146-5173.
105. Dazzi, A., et al., *AFM–IR: combining atomic force microscopy and infrared spectroscopy for nanoscale chemical characterization*. Applied spectroscopy, 2012. **66**(12): p. 1365-1384.
106. Jalan, I., et al., *AFM-IR spectromicroscopy unveils hidden phase separation in polymer–polymer blend films for photovoltaic applications*. ACS Applied Polymer Materials, 2024. **6**(18): p. 11312-11319.
107. Blazinic, V., et al., *Photo-degradation in air of spin-coated PC60BM and PC70BM films*. Synthetic metals, 2018. **241**: p. 26-30.
108. Watts, B., L. Thomsen, and P. Dastoor, *Methods in carbon K-edge NEXAFS: Experiment and analysis*. Journal of Electron Spectroscopy and Related Phenomena, 2006. **151**(2): p. 105-120.
109. Stöhr, J., *NEXAFS spectroscopy*. Vol. 25. 2013: Springer Science & Business Media.
110. Nefedov, A. and C. Wöll, *Advanced applications of NEXAFS spectroscopy for functionalized surfaces*, in *Surface Science Techniques*. 2013, Springer. p. 277-303.
111. Stöhr, J. and D. Outka, *Determination of molecular orientations on surfaces from the angular dependence of near-edge x-ray-absorption fine-structure spectra*. Physical Review B, 1987. **36**(15): p. 7891.

112. Stöhr, J., F. Sette, and A.L. Johnson, *Near-edge X-ray-absorption fine-structure studies of chemisorbed hydrocarbons: bond lengths with a ruler*. Physical review letters, 1984. **53**(17): p. 1684.
113. Horsley, J., et al., *Resonances in the K shell excitation spectra of benzene and pyridine: Gas phase, solid, and chemisorbed states*. The Journal of chemical physics, 1985. **83**(12): p. 6099-6107.
114. Benninghoven, A., *Surface analysis by secondary ion mass spectrometry (SIMS)*. Surface Science, 1994. **299**: p. 246-260.
115. Stephan, T., et al., *TOF-SIMS, applications in meteorite research, first results*. Meteoritics, Vol. 26, p. 397, 1991. **26**: p. 397.
116. Radicati di Brozolo, F., et al., *Imaging analysis of LDEF craters*. Meteoritics, Vol. 26, p. 387, 1991. **26**: p. 387.
117. Leng, Y., *Materials characterization: introduction to microscopic and spectroscopic methods*. 2013: John Wiley & Sons.
118. Vickerman, J.C. and D. Briggs, *ToF-SIMS: materials analysis by mass spectrometry*. 2013: im publications.
119. Cole, D.A. and L. Zhang, *Surface analysis methods for contaminant identification, in Developments in Surface Contamination and Cleaning*. 2008, Elsevier. p. 585-652.
120. Taylor, A.J., D.J. Graham, and D.G. Castner, *Reconstructing accurate ToF-SIMS depth profiles for organic materials with differential sputter rates*. Analyst, 2015. **140**(17): p. 6005-6014.
121. Seah, M. and A. Shard, *The matrix effect in secondary ion mass spectrometry*. Applied Surface Science, 2018. **439**: p. 605-611.

List of abbreviations and acronyms

A-D-A'-D-A	Acceptor - Donor – Acceptor' - Donor – Acceptor
AFM	Atomic Force Microscopy
AFM-IR	Atomic Force Microscopy – Infrared spectroscopy
BDD	benzo[1,2-b:4,5-c']-dithiophene-4,8-dione
BDT	benzo[1,2-b:4,5-b']-dithiophene
BHJ	Bulk Heterojunction
BT	Benzothiadiazole
CB	Chlorobenzene
CF	Chloroform
CPD	Contact Potential difference
CT	Charge Transfer
o-XYL	ortho-xylene
D-A	Donor – Acceptor
ETL	Electron Transport Layer
FF	Fill Factor
FY	Fluorescence Yield
GIWAXS	Grazing Incidence Wide Angle X-ray scattering
HTL	Hole Transport Layer
HOMO	Highest Occupied Molecular Orbital
ITO	Indium-tin-oxide
IR	Infrared
J _{sc}	Short-circuit Current
KPFM	Kelvin probe force microscopy
LUMO	Lowest Unoccupied Molecular Orbital
MO	Molecular Orbital
NEXAFS	Near-edge X-ray Absorption fine structure
NFA	Non-Fullerene Acceptor
OSC	Organic Solar Cells
PBDB-T	poly[(2,6-(4,8-bis(5-(2-ethylhexyl)thiophen-2-yl)-benzo[1,2-b:4,5-b']dithiophene))-alt-(5,5-(1',3'-di-2-thienyl-5',7'-bis(2-ethylhexyl)benzo[1',2'-c:4',5'-c']dithiophene-4,8-dione)]
pc-AFM	Photoconductive Atomic Force Microscopy
PC ₆₁ BM	[6,6]-Phenyl C ₆₁ butyric acid methyl ester
PCE	Power Conversion Efficiency
P _{in}	Power density of incident light
P _{max}	Maximum Power density output

Y6 2,20-((2Z,20Z)-((12,13-bis(2-ethylhexyl)-3,9-
diundecyl-12,13-dihydro-[1,2,5] thiadiazolo[3,4-e]thieno[2,"30':4',50]
thieno[20,30:4,5]pyrrolo[3,2-g] thieno[20,30:4,5]thieno[3,2-b]in-
dole-2,10-diyl)bis(methanylylidene)) bis(5,6-difluoro-3-oxo-2,3-di-
hydro-1H-indene-2,1-diylidene))dimalononitrile)



Molecular Orientation and Nanoscale Morphology-Property Relations in Organic Semiconductors for Photovoltaics

Organic solar cells (OSCs) are lightweight, flexible, scalable alternatives to traditional silicon solar panels. In OSCs, molecular semiconductors convert solar energy into electricity. With efficiencies exceeding 20%, OSCs have become a promising renewable energy technology.

The photoactive layer in a photovoltaic device is typically coated from a blend solution of electron-donor and electron-acceptor molecules. Recent development of new materials introduces new challenges in controlling and characterizing the morphology of the photoactive layer.

In this work, we use X-ray absorption spectroscopy to demonstrate that the choice of solvent used to process the photoactive layer plays an important role in determining the molecular orientation of the molecules. In addition, we introduced a novel approach that allows selective probing of the molecular orientation of the electron-acceptor in blended films. We also demonstrate that the deposition method can be used to control the vertical stratification in donor-acceptor systems. Complementary SPM techniques were applied to investigate the morphology-property relations at the nanoscale, highlighting both opportunities and challenges in the study of modern photoactive layers.

ISBN 978-91-7867-694-1 (print)

ISBN 978-91-7867-695-8 (pdf)

ISSN 1403-8099

DOCTORAL THESIS | Karlstad University Studies | 2026:23
